Reactive fluid flow topology optimization with the multi-relaxation time lattice Boltzmann method and a level-set function

Florian Dugast, Yann Favennec, Christophe Josset

Reactive fluid flow topology optimization with the multi-relaxation time lattice Boltzmann method and a level-set function

Florian DUGAST

Department of Mechanical Engineering and Materials Science, University of Pittsburgh, Benedum Hall, 3700 O'Hara Street, Pittsburgh, PA 15261

Yann FAVENNEC, Christophe JOSSET*

Laboratoire de Thermique et Énergie de Nantes, UMR CNRS 6607, La Chantrerie, Rue Christian Pauc, BP 50609, 44306 Nantes Cedex 03, France

* *corresponding author: christophe.josset@univ-nantes.fr*

Abstract

This paper presents a topology optimization algorithm based on the lattice Boltzmann method coupled with a level-set method for increasing the efficiency of reactive fluid flows. The multi-relaxation time model is considered for the lattice Boltzmann collision operator, allowing higher Reynolds numbers flow simulations compared to the ordinary single-relaxation time model. The cost function gradient is obtained with the derivation of the adjoint-state formulation for the fully coupled problem. The proposed method is tested successfully on several numerical applications involving Reynolds numbers from 10 up to 1,000, as well as with different Damkohler and Peclet numbers. A limitation of the maximal pressure drop is also applied. The obtained results demonstrate that the proposed numerical method is robust and efficient for solving topology optimization problems of reactive fluid flows, in different operating conditions.

Keywords: Topology optimization, adjoint-state formulation, reactive fluid flow, lattice Boltzmann method, level-set method

1. Introduction

The development of efficient reactors is needed in many chemical process and energy applications: chemical synthesis, catalytic combustion, and electro-chemical conversion, to cite but a few. The growth of renewable energy (wind, solar, or marine) implies an improvement of the electricity storage technologies. Electrolysers, or redox-flow batteries, can be used for the first stage of the electro-chemical conversion, and fuel cells for the reverse reactions. One of the principal characteristics to improve is the power density (kW/m^3, kW/m^2 or kW/kg) that represents the "good use" of the constitutive materials. All these systems can be seen as electrochemical reactors, where reactants are supplied to the reaction place by convection and diffusion mechanisms while by-products (thermal energy or new species) need to be removed (to avoid thermal problems or to leave free access to the reaction location). In the case of conventional vanadium redox-flow batteries, the reaction occurs on the material surface, whereas in the case of fuel cells, the species transport is more complicated. For example, in the case of polymer exchange membrane fuel cells (PEMFC), the reactants are usually transported into the gas channels and are diffused through a thin porous medium, in order to reach the catalyst layers (anode or cathode).

In this context, the efficiency of the reaction depends on the fluid flow channels geometry inside the domain. Some geometries have been tested in literature to this matter (serpentine [1], inter-digitated [2], etc.), but there are still discussions about which configuration is optimal, or the best, and benchmark parameters are not well-established [3]. Structural optimization techniques provide a promising method to overcome the strong limitation of determining *a priori* a system's geometry. Previous methods required this to be specified to allow optimization through testing relevant parameters (e.g. channel dimensions), significantly limiting the structural configurations possible.

Doing so, the fluid/solid distribution is to be determined via optimization methods. Among the three main optimization methods, namely the size optimization, the shape optimization, and the topology optimization [4], the latest is associated to the highest number of degrees of freedom. With topology optimization, very different geometries can be dealt with and obtained, leading to high levels of geometrical complexity, and with the ability of creating holes inside the domain of interest (this is not possible with either optimization strategies of size and shape optimization).

The basic idea of topology optimization is to optimize a material allocation problem where the material can have different properties. One of the first applications concerns the structural mechanical optimization, with compliance minimization [5, 6]. In that case, the material is either void or solid, but it can also be fluid or solid, in order to build fluid channels, for example. Topology optimization is well developed for fluid flow designs [7–10], but most often for solving pressure drop minimization problems.

One challenge of topology optimization is to develop multi-physics applications. As the complexity of the physics increases for these problems, topology optimization can be helpful to suggest innovative geometries that could not be intuitively thought. Although some topology optimization algorithms have been proposed for some heat transfer applications [11–15] , the development of such methods for chemical reaction is relatively scarce. Non exhaustively, the following works are of great interest. In their seminal publication, Okkels et al. [16] extended the work of Borrvall et al. [7] in the case of advection-diffusion-reaction problem. They worked on a catalytic microreactor for topology optimization and compared their results with empirical geometries, like a uniform or a membrane reactor. They also studied the influence of the relevant physical parameters on the optimized geometries. Schäpper et al. [17] dealt with topology optimization of bio reactors. They could show that the production of protein could be improved with topology optimization compared to a conventional reactor with a uniform distribution of biomass. A compromise is found for the glucose flowrate, sufficient enough for the reaction to happen and limited to avoid a strong ethanol production, which decreases the enzym activity. Yaji et al. [18] worked on vanadium redox flow batteries to provide a sufficient supply of species to the carbon fiber electrode, under a pressure drop constraint. The electrode is modeled as a porous medium with Darcy's law and the generation rate depends on the local velocity. The resulting optimal structure is an interdigitated flow field with strong tortuosity. This is due to the porous structure of the solid electrode, encouraging the flow through it in order to enhance the reaction. Kim et al. [19] worked on PEM fuel cells optimization in order to maximize the reaction rate between hydrogen and oxygen. Their topology optimization method has been applied to different geometry initializations such as centered inlet and outlet, multi-terminal inlet and outlet or serpentine channels.

In these three studies: [16–18], the catalyst for the reaction is located directly on the porous support, whereas in [19], the reaction takes place in the fluid channels. In this last application, the specificity of a PEM fuel cell with

different layers is taking into account: the optimization deals with the best way to feed reactant into a planar electrode and the solid has two functions: electrode supporting and fluid routing. The work presented in this article will follow the same approach. All the previously cited works rely on the SIMP modelization regarding the design material. This one is represented by a scalar field varying continuously from 0 (solid) to 1 (fluid). Intermediate states are penalized during the optimization process in order to promote a clear transition between the solid and the fluid. However, gray-scale effects occur, and, as mentioned by Makhija et al. [20], the porosity model does not prevent diffusion into and through solid regions, excluding low Peclet number simulations, when advection and diffusion are of the same order of magnitude. In order to overcome this issue, a level-set function (LSF) was used in this study for the fluid/solid representation. As the level-set function is continuous, it provides a continuous fluid/solid transition as required by the optimization process. However it is possible to use the zero contour of the LSF in order to get a clear fluid/solid interface. This latter feature is particularly interesting to obtain accurate boundaries for the forward problem. Many different methods can fall under a level-set appellation. Differing from the original work of Allaire [21], the evolution of the level-set function will not be realized with the Hamilton-Jacobi equation combined with shape derivatives. A similar approach to that of Yamada [22] was applied here, with no advection in the LSF evolution equation but only a source term depending on the design sensitivities. With this method, the LSF does not need to be re-initialized during the optimization process and the creation of discontinuity in the material distribution is also possible. A smooth Heaviside function is proposed for the calculation of the cost function gradient, and a threshold is then applied to compute the forward problem, with discrete 0-1 boundaries.

Next, all the works previously cited for the topology optimization of chemical process were based on a finite element strategy to solve both the Navier-Stokes equations and the advection-diffusion-reaction equation. As an alternative to ordinary discretization methods (finite element method (FEM), finite volume method (FVM)), the lattice Boltzmann method (LBM) may be very efficient for solving that kind of problem. Originally, this method has been used for fluid flow problems [23, 24] in which both the displacement and the collision of particles are solved via the Boltzmann equation, involving a (often simplified) collision operator. The macroscopic quantities for the flow field (density, pressure, velocity) can then be recovered by the

moments of the distribution function involved in the Boltzmann equation. Since the pioneering work of Pingen [25], adjoint-state LBM methods have also been developed for fluid flow identification [26, 27] or topology optimization [15, 28, 29]. It is also to be noticed that the LBM computational time of both forward and adjoint-state problems can be significantly reduced with GPU parallel computing [30–32]. Further, with the use of a uniform grid, the remeshing process may not be necessary along with the optimization iterations. This is another clear advantage of the LBM over FEM and FVM: it is indeed very convenient in topology optimization where the complex fluid/solid geometry evolves with the iterations of the optimization process. Also, the LBM boundary conditions are easy to implement (bounce-back at no-slip walls for example) making the LBM a good candidate if fluid/solid porous structures need to be computed, which can occur in topology optimization with the creation of complex geometries. Generally speaking, the LBM is convenient for multiphase flows, as the interface can be implicitly tracked with multiple distribution functions [33]. Though being beyond the scope of this article, such physics will be used in oncoming research.

In order to compute reactive flows, the concentration field is represented by a passive scalar quantity which is transported by the fluid flow. This quantity is computed in the LBM framework by a double distribution function approach [34, 35], more stable than multi-speed models [36]. Another distribution function is thus introduced to compute this concentration, in addition to the first distribution function used within the ordinary LBM related to the fluid flow only. Compared to the previous work done in LBM topology optimization in thermal fluid flow problems [15], a source term is introduced in this distribution function to represent the consumption of the reactant during the chemical reaction. Reaction laws are very numerous and can be highly nonlinear and multi-parameters dependent (for example Arrhenius law for the temperature dependence). In optimization literature, generally, the reactant equation has a linear dependence with the concentration. At the inlet, the reactant concentration is maximum, before decreasing inside the domain. The chemical reaction is then considered optimized when the reactant is fully consumed at the outlet. Mathematically speaking, this optimization problem consists in minimizing the mean concentration at the outlet. Obviously, one can seek not only for the full use of the reactant but also for the best use of reactant: many reaction problems require an homogeneous reaction rate, in order to avoid either over heating for exothermic reactions or catalyst aging. In this case the optimization is multi-objectives

(for example searching for an entire consumption of the reactant and an homogeneous reaction rate at the same time) and requires specific numerical methods; this problematic is beyond the scope of this publication.

In this article, a topology optimization method for an advection-diffusion reaction problem using the lattice Boltzmann method and a level-set function is presented. A multiple relaxation time operator is used to compute fluid flows with Reynolds numbers up to 1,000 and for different Schmidt numbers (ratio between the momentum diffusion and the mass diffusion) [20]. As this study depends on several physical parameters (flow regime, reactant mass diffusivity, reaction rate), their influence on the forward problem and on the optimized geometry is also investigated. A limitation of the pressure drop is also introduced in the optimization problem as a constraint.

The paper is organized as follows. Section 2 introduces the main features of the topology optimization method including the update of the geometry with a level-set function. Section 3 presents the background theory for LBM and its application for an advection-diffusion reaction equation. This forward problem is eventually written down concisely in residual form, and the cost function to be minimized is also rewritten in terms of lattice Boltzmann variables. Section 4 presents the derivation of the cost function gradient through the adjoint-state method. The concise residual form is again given. Section 5 then presents the numerical examples related to the topology optimization of an advection-diffusion reaction problem. The geometry of the problem is a 2D square cavity with the inlet close to the top-left corner and the outlet close to the bottom-right corner; the reaction occurs in the entire domain. This academic test case is a variation of the 2D cavity studied by Okkels and Bruus [16], but the methodology presented in the current paper can be extended to real-life applications and 3D configurations. First, a study about the influence of the Reynolds number is presented with Reynolds numbers from 10 to 1,000. This range is chosen to explore solutions at sufficiently high Reynolds numbers to have a benefit in stability with the MRT-LBM model used here, while focusing on the laminar regime to maintain the validity of the model. Then the influence of the other physical parameters (Peclet or Damkholer numbers) is also discussed. All the obtained results demonstrate that the proposed numerical method is robust and efficient for solving topology optimization problems of reactive fluid flows, in various operating conditions. Some discussions and conclusions are finally drawn in section 6.

2. Definition of the optimization problem

2.1. The physics of advection-diffusion-reaction

The chemical species are transported by the fluid flow and the reaction is taken into account by a source term involved in the equation of the species concentration. This problem is written with the following macroscopic equations $\forall \boldsymbol{x} \in \mathcal{D}$, $\mathcal{D}$ being an open bounded set of $\mathbb{R}^2$:

$$\nabla \cdot \boldsymbol{u} = 0, \tag{1}$$

$$(\boldsymbol{u} \cdot \nabla)\, \boldsymbol{u} + \frac{1}{\rho} \nabla p - \nu \nabla^2 \boldsymbol{u} = 0, \tag{2}$$

$$\boldsymbol{u} \cdot \nabla c_A - D \nabla^2 c_A + s = 0. \tag{3}$$

The source term s involved in eq. (3) is expressed as a function of the concentration of the species of concern, $c_A = [A] = \frac{n_A}{V}$. One possibility is to express a linear dependency between s and c_A, as in [19]. Elsewhere, in [17] and [18], the reaction rate is limited by the ethanol production, or by the velocity field, meaning that the reaction rate reaches a maximum value k for a specific concentration. Many other models can be used depending on the chemical reactions, using linear, quadratic, cubic, logarithmic, or exponential relations, to cite but a few [37, 38]. With a linear source term, $s = k\, c_A$, when introducing a given characteristic length of the computational domain L, and a characteristic velocity U into the initial set of equations eqs. (1) to (3), and combining the three physical parameters, namely the fluid viscosity, ν, the mass diffusivity of the chemical species, D, and the maximal reaction rate, k, one can recover the classical dimensionless version of the initial problem:

$$\widetilde{\nabla} \cdot \widetilde{\boldsymbol{u}} = 0, \tag{4}$$

$$\left(\widetilde{\boldsymbol{u}} \cdot \widetilde{\nabla}\right) \widetilde{\boldsymbol{u}} + \widetilde{\nabla} \widetilde{p} - \frac{1}{\mathrm{Re}} \widetilde{\nabla}^2 \widetilde{\boldsymbol{u}} = 0, \tag{5}$$

$$\widetilde{\boldsymbol{u}} \cdot \widetilde{\nabla} \widetilde{c}_A - \frac{1}{\mathrm{Pe}} \widetilde{\nabla}^2 \widetilde{c}_A + \mathrm{Da}\, \widetilde{c}_A = 0. \tag{6}$$

Here tilde values $\widetilde{X}$ stand for dimensionless version of X and the three dimensionless numbers Re, Sc and Da are defined as follow:

- the Reynolds number, $\mathrm{Re} = \frac{UL}{\nu}$, represents the ratio between inertial and viscous forces involved in a fluid flow. It can help to distinguish flow regimes, from laminar to turbulent flows;

- the Schmidt number, $\mathrm{Sc} = \frac{\nu}{D}$, is the ratio of the kinematic viscosity (momentum diffusivity) over the mass diffusivity;
- the Damkohler number, $\mathrm{Da} = \frac{kL}{U}$, represents the ratio of the reaction rate over the transport phenomena rate in the system.

Alternatively, the Peclet number can be used, $\mathrm{Pe} = \mathrm{Re} \times \mathrm{Sc}$. It represents the ratio between the transfer by convection and the transfer by diffusion.

In fluid flow topology optimization problems, the principal effect of modifying the topology is the modification of the velocity distribution. It means that for the optimization to be effective, the convection process has to play a major role for the concentration distribution when compared to the diffusion process. Otherwise, the influence of the advection process on the efficiency of the chemical reaction would be too small. So a high Peclet number is chosen here to respect this condition. However, diffusion dominant processes can also be optimized using this method but the problem will be simpler by removing eqs. (1) to (2) to the set of equations to be solved. About the reaction rate, a compromise is to be found: if the reaction rate represented by the Damkohler number is too high, the reactant is consumed too fast in the domain, and, there is no need of using any topology optimization algorithms. Completely on the other hand, if the reactant is consumed too slowly, then the concentration gradients are too small and the impact of the fluid/solid geometry will also be negligible. For these two extreme cases, the optimization problem is insensitive because of the bad sizing of the space domain $\mathcal{D}$: this one has to be decreased (resp increased) in order to improve the sensitivity of the physical problem to the topology of the domain. In all cases in between, for ordinary reaction rates, the use of topology optimization may be very impact-full.

2.2. Setting up the optimization problem: reaction maximization

In topology optimization, one searches for the best material distribution – or at least a good enough distribution – to satisfy a given objective. The material distribution is represented by the design variable, and the objective is defined in terms of a cost function, $\mathcal{J}$. The update of the geometry will be obtained by the evolution of a level-set function, involving the cost function gradient. This gradient is given by the derivative of the cost function $\mathcal{J}$ with respect to the design variable. Section 4 is dedicated to such a derivation. The objective of the optimization problem is the maximization of the reaction, which is equivalent to the minimization of the product of the velocity

with the concentration, at the outlet of the domain. Mathematically, this is written as:

$$\mathcal{J} = \frac{1}{|\partial\mathcal{D}_{\text{out}}|}\int_{\partial\mathcal{D}_{\text{out}}} \boldsymbol{u}\cdot\boldsymbol{n}\; c_A \; + D\nabla c_A\cdot\boldsymbol{n}\;\mathrm{d}\boldsymbol{x}, \tag{7}$$

where $\boldsymbol{n}$ is the outward unit normal vector to the boundary, the first term of the integral is the convective part of the reactant flux while the second term represents the diffusive component. As the Pe number is far greater than one in all simulations, the diffusive component is neglected in this work.

A constraint is also to be added to the optimization problem in order to allow a maximum amount of pressure drop during the optimization process. Such a limitation is useful to prevent from unfeasible designs. Rather than adding inequality constraints on the optimization problem, a penalization term is added to the cost function, as in [39], in structural optimization, for example. The augmented cost function, $\mathcal{J}^+$, to be minimized, is thus:

$$\mathcal{J}^+ = \mathcal{J} + \ell\mathcal{J}_1 \quad \text{with} \quad \mathcal{J}_1 = \Delta p_{\max}\exp\left(\frac{\Delta p}{\Delta p_{\max}}\right), \tag{8}$$

and $\ell \in \mathbb{R}^+$ is a user-defined value controlling the relative importance of the different contributions $\mathcal{J}$ and $\mathcal{J}_1$.

2.3. Geometry update

The design domain is divided into N elements and there is one design parameter per element. The topology is represented by the signed variable $\alpha(\boldsymbol{x}) \in \mathbb{R}^N$. Then the level-set method is used for the mapping of the design variable. Such a method has been firstly implemented for the representation of interfaces in multiphase flows [40] and for image segmentation [41]. It has then been used for topology optimization, by Sethian et al. [42], Wang et al. [43], and Allaire et al. [44].

The continuous level-set function, is such that its zero contour defines the interface between the two media. The update of the solid/fluid distribution α is thus performed in two steps. The first one is via the evolution of the discrete level-set function $\Psi(\boldsymbol{x}) \in \mathbb{R}^N$:

$$\Psi^{(n+1)}(\boldsymbol{x}) = \Psi^{(n)}(\boldsymbol{x}) - \mathbf{P}^{(n)}\nabla_\Psi\mathcal{J}^{+(n)}(\boldsymbol{x}). \tag{9}$$

The superscript is the iteration count, $\mathbf{P}$ is the iteration matrix, ideally a good approximation of the inverse of the Hessian matrix, $\mathbf{P} \approx \widetilde{\mathbf{H}}^{-1}$, and $\nabla_\Psi\mathcal{J}^+$ is the augmented cost function gradient (this vector contains the

derivatives of the cost function with respect to all components of Ψ). The second step is the topology update which consists in applying the mapping between the level-set function and the topology.

In a previous study, the mapping from the level set function to the topology was defined as [15]:

$$\alpha(\Psi(\boldsymbol{x})) = \frac{1}{2}\left(1 + \text{sign}\Psi(\boldsymbol{x})\right), \tag{10}$$

such that

$$\alpha(\boldsymbol{x}) = \begin{cases} 0 & \text{if } \Psi(\boldsymbol{x}) < 0; \\ 1 & \text{if } \Psi(\boldsymbol{x}) > 0. \end{cases} \tag{11}$$

A smooth version of the mapping can be considered, for example [45]:

$$\alpha_\epsilon(\Psi(\boldsymbol{x})) = \frac{1}{2} + \frac{1}{\pi}\arctan\frac{\Psi(\boldsymbol{x})}{\epsilon}. \tag{12}$$

The main interest in using (12) rather than (10) is that the former is a continuous and differentiable function, with $\alpha'_\epsilon(\Psi)$ finite everywhere, as soon as $\epsilon \neq 0$. Besides, if $\epsilon \to 0$, a clear discontinuous fluid/solid interface is obtained, which is useful while solving the forward problem. Indeed, the LBM implementation used here for the fluid flow and for the concentration field does not involve a force term to deal with a Brinkmann penalization for a porous media. As a consequence, each node must be either strictly fluid or solid, and no intermediate state is allowed. It means that a threshold is applied after the update of the level-set function to obtain a clear fluid/solid interface for the forward problem. The choice of this parameter ϵ is discussed in the section dedicated to numerical results. In the following, the subscript ϵ is avoided for readability considerations.

Note that other strategies such as the Brinkmann penalization for modeling the porous medium, coupled with the SIMP method could have been used [20]. However, the level-set function allows a clearer definition of the topology, and thus minimizes the possible bias involved within the forward model.

3. Lattice Boltzmann method

3.1. Multi-relaxation time model for the fluid flow

The lattice Boltzmann method (LBM) is an alternative way of solving fluid flow problems compared to classical methods based on the discretization of the Navier–Stokes equations (finite volume or finite element methods). This method is based on the calculation of the distribution function f involved in the Boltzmann equation and which gives the probability of finding a particle at the position $\boldsymbol{x}$, at the time t and at the speed $\boldsymbol{c}$. Compared to the Boltzmann equation, the velocity vector is discretized along directions in the lattice Boltzmann equation, such as [46, 47]:

$$\frac{\partial f_i}{\partial t} + \boldsymbol{c}_i \cdot \nabla f_i = \Omega_i(\boldsymbol{f}) \quad \forall i \in [\![0; I-1]\!]. \tag{13}$$

The notation $\boldsymbol{f} = \{f_i\}_{i=0}^{I-1}$ will be used for the distribution function. Such a notation will be used for other quantities, as soon as there is no possible ambiguity. In two dimensions, the reference discretization scheme involves $I = 9$ discrete directions – yielding the so-called D2Q9 scheme. The directions and associated weights are given by [48]:

$$\boldsymbol{c} = \begin{pmatrix} 0 & 1 & 0 & -1 & 0 & 1 & -1 & -1 & 1 \\ 0 & 0 & 1 & 0 & -1 & 1 & 1 & -1 & -1 \end{pmatrix}, \tag{14}$$

$$\boldsymbol{w} = \begin{pmatrix} \frac{4}{9} & \frac{1}{9} & \frac{1}{9} & \frac{1}{9} & \frac{1}{9} & \frac{1}{36} & \frac{1}{36} & \frac{1}{36} & \frac{1}{36} \end{pmatrix}. \tag{15}$$

Also, from the definition of the velocity directions, it is convenient to introduce the opposed velocity directions $\bar{\boldsymbol{i}}$ with respect to $\boldsymbol{c}_0$, to write the bounce-back boundary conditions:

$$\bar{\boldsymbol{i}} = \begin{pmatrix} \bar{0} & \bar{1} & \bar{2} & \bar{3} & \bar{4} & \bar{5} & \bar{6} & \bar{7} & \bar{8} \end{pmatrix} = \begin{pmatrix} 0 & 3 & 4 & 1 & 2 & 7 & 8 & 5 & 6 \end{pmatrix}. \tag{16}$$

The lattice Boltzmann equation (13) is generally solved in two steps: the collision step, and the streaming step. For the collision operator, $\Omega(\boldsymbol{f})$, the simple model introduced by Bhatnagar-Gross-Krook (BGK) [49, 50] which relies on a single-relaxation time (SRT) is often used. However, this is often a source of spurious oscillations and instabilities as the Reynolds number increases. As an example, d'Humières et al. [51] reported severe oscillations for the pressure field in the cavity flow for the SRT model at Re=500. So,

in order to improve the numerical stability of the LBM, a multi-relaxation time (MRT) operator has further been introduced [51]. It is written as:

$$\Omega(\boldsymbol{f}) = -\mathbf{M}^{-1}\mathbf{S}\mathbf{M}\left(\boldsymbol{f} - \boldsymbol{f}^{\mathrm{eq}}\right), \tag{17}$$

in which $\mathbf{M}$ is the transformation matrix between the moments and the distribution functions:

$$\mathbf{M} = \begin{pmatrix} 1 & 1 & 1 & 1 & 1 & 1 & 1 & 1 & 1 \\ -4 & -1 & -1 & -1 & -1 & 2 & 2 & 2 & 2 \\ 4 & -2 & -2 & -2 & -2 & 1 & 1 & 1 & 1 \\ 0 & 1 & 0 & -1 & 0 & 1 & -1 & -1 & 1 \\ 0 & -2 & 0 & 2 & 0 & 1 & -1 & -1 & 1 \\ 0 & 0 & 1 & 0 & -1 & 1 & 1 & -1 & -1 \\ 0 & 0 & -2 & 0 & 2 & 1 & 1 & -1 & -1 \\ 0 & 1 & -1 & 1 & -1 & 0 & 0 & 0 & 0 \\ 0 & 0 & 0 & 0 & 0 & 1 & -1 & 1 & -1 \end{pmatrix}, \tag{18}$$

and $\mathbf{S}$ is the diagonal relaxation rate matrix defined by [52]:

$$\mathbf{S} = \mathrm{diag}(1, s_e, s_\epsilon, 1, s_q, 1, s_q, s_\nu, s_\nu). \tag{19}$$

Note that $s_i = 1$ corresponds to conserved moments (conservation of mass and momentum), and s_ν is related to the fluid viscosity:

$$\frac{1}{s_\nu} = 3\nu + \frac{1}{2}. \tag{20}$$

The other components are to be adjusted in order to improve the numerical stability and are often determined to be close to one through an optimization process [53, 54]. In this article the fluid used in the cavity is water, so an incompressible model is used for the LBM. The equilibrium distribution f_i^{eq} is then given by [55, 56]:

$$f_i^{\mathrm{eq}} = \omega_i \left(\rho + \rho_0 \left(3\alpha(\boldsymbol{c}_i \cdot \boldsymbol{u}) + \frac{9}{2}\alpha(\boldsymbol{c}_i \cdot \boldsymbol{u})^2 - \frac{3}{2}\alpha \boldsymbol{u}^2 \right) \right). \tag{21}$$

The design-related variable $\alpha(\psi(\boldsymbol{x}))$ involved in eq. (21) has been defined in section 2. The macroscopic quantities, the fluid density ρ, the velocity $\boldsymbol{u}$, and the pressure can further be computed with the moments of $\boldsymbol{f}$:

$$\rho(\boldsymbol{x}, t) = \sum_{i=0}^{8} f_i(\boldsymbol{x}, t), \quad \rho_0 \boldsymbol{u}(\boldsymbol{x}, t) = \sum_{i=0}^{8} \boldsymbol{c}_i f_i(\boldsymbol{x}, t), \quad p(\boldsymbol{x}, t) = c_s^2 \rho(\boldsymbol{x}, t), \tag{22}$$

where $\rho = \rho_0 + \delta\rho$, $\delta\rho$ being the density fluctuation and the mean density ρ_0 is chosen to be equal to 1 in our simulations [56], and $c_s = 1/\sqrt{3}$ the lattice speed of sound. The fluid velocity needs to be very low compared to c_s in order to satisfy the low mach number assumption required for the equilibrium distribution function expansion [57]. Compared to the classical model, neglecting the density fluctuations in terms involving velocity induces a decoupling between density and velocity [58]. While reducing the errors due to compressibility [59], it should be noted that this model is only valid for steady-state flows [60]. Next, the bounce-back boundary condition is applied on all interfaces but on the inlet and outlet, where the boundary conditions proposed by Zou and He [24] are applied. The user-parameter ϵ involved in (12) is chosen to tend to zero within this multi-relaxation time lattice Boltzmann model, so that α equals either 0 or 1, and a clear definition of the topology is considered to avoid any bias in the fluid flow forward modeling.

3.2. Single-relaxation time model for the concentration distribution

Based on a double distribution function approach, a second distribution function, $\boldsymbol{g}$, similar to $\boldsymbol{f}$, is introduced to solve the concentration field [34, 35]:

$$\frac{\partial g_i}{\partial t} + \boldsymbol{c}_i \cdot \nabla g_i + s_i = \Omega_i \quad \forall i \in [\![0; I-1]\!], \tag{23}$$

with the collision operator defined as:

$$\Omega_i = -\frac{1}{\tau_g}\left(g_i - g_i^{\mathrm{eq}}\right). \tag{24}$$

Although the multi-relaxation time collision operator is used for the distribution function $\boldsymbol{f}$, the simpler single-relaxation time model is used here, with only one relaxation time τ_g for the distribution function $\boldsymbol{g}$. The lattice Boltzmann equation for the concentration is more stable than the one for the fluid flow, and the multi-relaxation time model is not mandatory for this distribution function.Indeed, the SRT-BGK model is suitable to solve this problem as long as the diffusion is isotropic [61, 62], which is the case here. The relaxation time τ_g is related to the mass diffusivity D of the chemical species:

$$\tau_g = 3D + \frac{1}{2}. \tag{25}$$

In (23), the source term involved in the reaction process equation is distributed on all the discrete velocity directions, according to the D2Q9 scheme.

For a linear source term, $s = k\,c_A$, one can write:

$$s_i = \omega_i\, k\, c_A \quad \forall i \in [\![0; I-1]\!]. \tag{26}$$

More generally, the LBM formulation for a given source model s is relaxed towards the different velocities directions as follow:

$$s_i = \omega_i\, s. \tag{27}$$

The equilibrium distribution function g_i^{eq} is given by [63]:

$$g_i^{eq} = \omega_i\, c_A \left(1 + 3\alpha\ \boldsymbol{c}_i \cdot \boldsymbol{u}\right). \tag{28}$$

It can be noticed that the velocity field is used to compute this equilibrium distribution function, illustrating the coupling between the concentration and the velocity.The concentration c_A is computed with the zeroth order of the distribution function $\boldsymbol{g}$ such as [35] :

$$c_A(\boldsymbol{x}, t) = \sum_{i=0}^{8} g_i(\boldsymbol{x}, t) \tag{29}$$

The mass flux is written as [14]:

$$\boldsymbol{q}(\boldsymbol{x}, t) = \sum_{i=0}^{8} \boldsymbol{c}_i g_i(\boldsymbol{x}, t) - c_A \boldsymbol{u} \tag{30}$$

In order to implement the boundary conditions, the unknown distribution functions are assumed to be the equilibrium distribution functions with the concentration $c_A^{'}$ to be determined [15, 64]. For the prescribed inlet concentration, $c_A^{'}$ is calculated by (29), with $c_A = c_{A\mathrm{in}}$. At the outlet, $c_A^{'}$ is calculated by (30), with $\boldsymbol{q} = 0$.

A similar solver has been validated for a fluid flow and heat transfer problem by the authors [32]. In that case, the passive scalar approach is also used, the only difference is that the concentration is replaced by the temperature.

3.3. Residual form

In order to calculate the cost function gradient, the adjoint-state method will be used, see section 4. In order to set it up, the forward problem, which consists of both the multi-relaxation time model for the fluid-flow, and the single-relaxation time model for the concentration distribution, is written down in terms of residuals. We denote R and P the residuals for the Boltzmann state equations, and the boundary conditions, respectively. Further, we use the superscripts f and g for the fluid flow, and for the concentration, respectively. Such residuals have to be written down for each velocity direction. Added to that, the boundary $\partial\mathcal{D}$ of the medium $\mathcal{D}$ is partitioned with the inlet $\mathcal{D}_{\text{in}}$, the outlet $\mathcal{D}_{\text{out}}$, and the no-slip boundaries $\mathcal{D}_{\text{ns}}$. With such notations, the forward problem is concisely written as:

$$
\begin{aligned}
&\text{search } (f_i, g_i)(\boldsymbol{x}, t),\ i \in [\![0, ..., 8]\!] \text{ such that:}\\
&\bullet\ \forall \boldsymbol{x} \in \mathcal{D}:\\
&\quad R_i^f(\boldsymbol{f}, \alpha) = \tfrac{\partial f_i}{\partial t} + \boldsymbol{c}_i \cdot \nabla f_i + \left(\mathbf{M}^{-1}\mathbf{S}\mathbf{M}\left(\boldsymbol{f} - \boldsymbol{f}^{\text{eq}}\right)\right)_i = 0,\\
&\quad R_i^g(\boldsymbol{f}, \boldsymbol{g}, \alpha) = \tfrac{\partial g_i}{\partial t} + \boldsymbol{c}_i \cdot \nabla g_i + s_i + \tfrac{1}{\tau_g}\left(g_i - g_i^{\text{eq}}\right) = 0,\\
&\bullet\ \forall \boldsymbol{x} \in \partial\mathcal{D}_{\text{in}}:\\
&\quad P_1^f(\boldsymbol{f}) = f_1 - f_3 - \tfrac{2}{3}u_{\text{in}} = 0,\\
&\quad P_5^f(\boldsymbol{f}) = f_5 - f_7 - \tfrac{1}{6}u_{\text{in}} - \tfrac{1}{2}(f_4 - f_2) = 0,\\
&\quad P_8^f(\boldsymbol{f}) = f_8 - f_6 - \tfrac{1}{6}u_{\text{in}} + \tfrac{1}{2}(f_4 - f_2) = 0,\\
&\quad P_1^g(\boldsymbol{g}) = g_1 - \tfrac{1}{9}\chi\left(1 + 3u_{\text{in}}\right) = 0,\\
&\quad P_5^g(\boldsymbol{g}) = g_5 - \tfrac{1}{36}\chi\left(1 + 3u_{\text{in}}\right) = 0,\\
&\quad P_8^g(\boldsymbol{g}) = g_8 - \tfrac{1}{36}\chi\left(1 + 3u_{\text{in}}\right) = 0,\\
&\bullet\ \forall \boldsymbol{x} \in \partial\mathcal{D}_{\text{out}}:\\
&\quad P_3^f(\boldsymbol{f}) = f_3 - f_1 + \tfrac{2}{3}\eta = 0,\\
&\quad P_6^f(\boldsymbol{f}) = f_6 - f_8 + \tfrac{1}{6}\eta - \tfrac{1}{2}\left(f_4 - f_2\right) = 0,\\
&\quad P_7^f(\boldsymbol{f}) = f_7 - f_5 + \tfrac{1}{6}\eta + \tfrac{1}{2}\left(f_4 - f_2\right) = 0,\\
&\quad P_3^g(\boldsymbol{f}, \boldsymbol{g}) = g_3 - \tfrac{1}{9}\zeta\left(1 - 3\eta\right) = 0,\\
&\quad P_6^g(\boldsymbol{f}, \boldsymbol{g}) = g_6 - \tfrac{1}{36}\zeta\left(1 - 3\eta\right) = 0,\\
&\quad P_7^g(\boldsymbol{f}, \boldsymbol{g}) = g_7 - \tfrac{1}{36}\zeta\left(1 - 3\eta\right) = 0,\\
&\bullet\ \forall \boldsymbol{x} \in \partial\mathcal{D}_{\text{ns}}:\\
&\quad P^f_{(\boldsymbol{c}_i\cdot\boldsymbol{n}<0)}(\boldsymbol{f}) = f_{(\boldsymbol{c}_i\cdot\boldsymbol{n}<0)} - f_{(\bar{\boldsymbol{c}_i}\cdot\boldsymbol{n}>0)} = 0,\\
&\quad P^g_{(\boldsymbol{c}_i\cdot\boldsymbol{n}<0)}(\boldsymbol{g}) = g_{(\boldsymbol{c}_i\cdot\boldsymbol{n}<0)} - g_{(\bar{\boldsymbol{c}_i}\cdot\boldsymbol{n}>0)} = 0,
\end{aligned}
\tag{31}
$$

with:

$$\begin{aligned}
&\eta = -\rho_{\text{out}} + f_0 + f_2 + f_4 + 2(f_1 + f_5 + f_8),\\
&\chi = \tfrac{6(c_{A\,\text{in}} - g_0 - g_2 - g_3 - g_4 - g_6 - g_7)}{(1+3u_{\text{in}})},\\
&\zeta = \tfrac{6(g_1+g_5+g_8)}{(1+3\eta)}.
\end{aligned} \tag{32}$$

3.4. LBM-based cost function

The cost function written in terms of the primal variables is given combining eqs. (7) and (8), which gives:

$$\mathcal{J}^+\left(\boldsymbol{u}, c_A, \Delta p\right) = \frac{1}{|\partial\mathcal{D}_{\text{out}}|}\int_{\partial\mathcal{D}_{\text{out}}} \boldsymbol{u}\cdot\boldsymbol{n}\; c_A\; \mathrm{d}\boldsymbol{x} + \ell\Delta p_{\max}\exp\left(\frac{\Delta p}{\Delta p_{\max}}\right). \tag{33}$$

This cost function is to be re-written in terms of the lattice Boltzmann variables, $\boldsymbol{f}$ and $\boldsymbol{g}$. Taking into account of the following relationships between the primal variables and the lattice Boltzmann variables:

$$\begin{aligned}
&\boldsymbol{u} = \textstyle\sum_{i=0}^{8} \boldsymbol{c}_i f_i(\boldsymbol{x}, t)\\
&c_A = \textstyle\sum_{i=0}^{8} g_i(\boldsymbol{x}, t)\\
&\Delta p = \tfrac{1}{|\partial\mathcal{D}_{\text{in}}|}\left[\tfrac{1}{3}\int_{\partial\mathcal{D}_{\text{in}}}\textstyle\sum_{i=0}^{8} f_i\,\mathrm{d}\boldsymbol{x} - \tfrac{1}{3}\int_{\partial\mathcal{D}_{\text{out}}}\textstyle\sum_{i=0}^{8} f_i\,\mathrm{d}\boldsymbol{x}\right],
\end{aligned} \tag{34}$$

the cost function that is, finally, to be minimized is:

$$\begin{aligned}
\widehat{\mathcal{J}}^+\left(\boldsymbol{f}, \boldsymbol{g}\right) = &\frac{1}{|\partial\mathcal{D}_{\text{out}}|}\int_{\partial\mathcal{D}_{\text{out}}}\sum_{i=0}^{8}\boldsymbol{c}_i f_i\cdot\boldsymbol{n}\;\sum_{i=0}^{8} g_i\;\mathrm{d}\boldsymbol{x}\\
&+ \ell\Delta p_{\max}\exp\left(\frac{\frac{1}{3}\int_{\partial\mathcal{D}_{\text{in}}}\sum_{i=0}^{8} f_i\,\mathrm{d}\boldsymbol{x}}{|\partial\mathcal{D}_{\text{in}}|\,\Delta p_{\max}}\right).
\end{aligned} \tag{35}$$

Note that the pressure term at the outlet is not involved here. This one being considered as prescribed, the pressure difference is only driven by the modification of the inlet pressure during the optimization.

4. The cost function gradient

In order to derive the full adjoint-state problem needed for the computation of the cost function gradient, the methodology and notations of Gunzburger [65] are introduced:

- $\boldsymbol{F}(\boldsymbol{\phi}, \Psi) = 0$ is the forward model gathering all the equations of eq. (31);
- $\boldsymbol{\phi} = (\boldsymbol{f}, \boldsymbol{g})$ is the global forward state;
- $\boldsymbol{\phi}^* = (\boldsymbol{f}^*, \boldsymbol{g}^*)$ is the global adjoint-state.

The Lagrange function associated to the optimization problem is written as[1]:

$$\mathcal{L}\left(\boldsymbol{\phi}, \Psi, \boldsymbol{\phi}^*\right) = \widehat{\mathcal{J}}^+(\boldsymbol{\phi}) + \left\langle \boldsymbol{F}(\boldsymbol{\phi}, \Psi), \boldsymbol{\phi}^* \right\rangle . \tag{37}$$

The optimization problem is solved searching for the stationary point of the Lagrange function. This point satisfies:

$$\delta\mathcal{L} = \frac{\partial \mathcal{L}}{\partial \boldsymbol{\phi}} \delta\boldsymbol{\phi} + \frac{\partial \mathcal{L}}{\partial \Psi} \delta\Psi + \frac{\partial \mathcal{L}}{\partial \boldsymbol{\phi}^*} \delta\boldsymbol{\phi}^* = 0, \tag{38}$$

where $\delta\mathcal{L}$, $\delta\boldsymbol{\phi}$, $\delta\Psi$ and $\delta\boldsymbol{\phi}^*$ stand for arbitrary variations [65]. Three terms appear in the right hand side of (38):

- the first term, the differential with respect to the state, $\partial\mathcal{L}/\partial\boldsymbol{\phi}$, yields the adjoint-state equation;
- the second term, the differential with respect to the design variables, $\partial\mathcal{L}/\partial\Psi$, yields the optimality conditions;

[1] With the notations given above, this eq. (37) can be straitforwardly expanded to:

$$\begin{aligned}\mathcal{L}(\boldsymbol{f}, \boldsymbol{g}, \Psi, \boldsymbol{f}^*, \boldsymbol{g}^*) = \widehat{\mathcal{J}}^+(\boldsymbol{f}, \boldsymbol{g}) + \int_0^{t_f} \Bigg(\int_{\mathcal{D}} \sum_{\substack{q=\{f,g\} \\ i=0,\dots,8}} R_i^q \; q_i^* \; \mathrm{d}\boldsymbol{x} \\ + \left(\int_{\partial\mathcal{D}_{\text{in}}} \sum_{\substack{q=\{f,g\} \\ i=\{1,5,8\}}} + \int_{\partial\mathcal{D}_{\text{out}}} \sum_{\substack{q=\{f,g\} \\ i=\{3,6,7\}}} + \int_{\partial\mathcal{D}_{\text{ns}}} \sum_{\substack{q=\{f,g\} \\ \boldsymbol{c}_i \cdot \boldsymbol{n} < 0}} \right) \left(P_i^q \; q_i^* \; \mathrm{d}\boldsymbol{x} \right) \Bigg) \mathrm{d}t. \end{aligned} \tag{36}$$

- the third term, the differential with respect to the adjoint-state variable, $\partial\mathcal{L}/\partial\boldsymbol{\phi}^*$, yields back the equations of the forward model that are to be satisfied.

A similar derivation of the adjoint-state problem for a convective fluid flow problem has been detailed by the authors [15]. Based on this method, the adjoint-state is finally written as :

search $(f_i^*, g_i^*)(\boldsymbol{x}, t),\ i \in [\![0, ..., 8]\!],$ with $(f_i, g_i)(\boldsymbol{x}, t)$ given by (31), such that:

- $\forall \boldsymbol{x} \in \mathcal{D}$:

$$R_i^{*,f}(\boldsymbol{f}, \boldsymbol{g}, \boldsymbol{f}^*, \boldsymbol{g}^*, \alpha) = -\frac{\partial f_i^*}{\partial t} - \boldsymbol{c}_i \cdot \nabla f_i^* + \left(\mathbf{M}^{-1}\mathbf{S}\mathbf{M}\left(\boldsymbol{f}^* - \boldsymbol{f}^{*,\mathrm{eq}}\right)\right)_i + Q_i^{*,f} = 0,$$
$$R_i^{*,g}(\boldsymbol{f}, \boldsymbol{g}, \boldsymbol{g}^*, \alpha) = -\frac{\partial g_i^*}{\partial t} - \boldsymbol{c}_i \cdot \nabla g_i^* + \frac{1}{\tau_g}\left(g_i^* - g_i^{*,eq}\right) + Q_i^{*,g} = 0,$$

- $\forall \boldsymbol{x} \in \partial\mathcal{D}_{\mathrm{in}}$:

$$P_3^{*,f}(\boldsymbol{f}^*, \boldsymbol{f}) = f_3^* - f_1^* + \ell\, \frac{1}{3|\partial\mathcal{D}_{\mathrm{in}}|} \exp\left(\frac{\frac{1}{3}\int_{\partial\mathcal{D}_{\mathrm{in}}} \sum_{i=0}^{8} f_i \,\mathrm{d}\boldsymbol{x}}{|\partial\mathcal{D}_{\mathrm{in}}|\Delta p_{max}}\right)$$
$$P_7^{*,f}(\boldsymbol{f}^*, \boldsymbol{f}) = f_7^* - f_5^* + \ell\, \frac{1}{3|\partial\mathcal{D}_{\mathrm{in}}|} \exp\left(\frac{\frac{1}{3}\int_{\partial\mathcal{D}_{\mathrm{in}}} \sum_{i=0}^{8} f_i \,\mathrm{d}\boldsymbol{x}}{|\partial\mathcal{D}_{\mathrm{in}}|\Delta p_{max}}\right)$$
$$P_6^{*,f}(\boldsymbol{f}^*, \boldsymbol{f}) = f_6^* - f_8^* + \ell\, \frac{1}{3|\partial\mathcal{D}_{\mathrm{in}}|} \exp\left(\frac{\frac{1}{3}\int_{\partial\mathcal{D}_{\mathrm{in}}} \sum_{i=0}^{8} f_i \,\mathrm{d}\boldsymbol{x}}{|\partial\mathcal{D}_{\mathrm{in}}|\Delta p_{max}}\right)$$
$$P_3^{*,g}(\boldsymbol{g}^*) = g_3^* + \frac{1}{6}\left(4g_1^* + g_5^* + g_8^*\right)$$
$$P_6^{*,g}(\boldsymbol{g}^*) = g_6^* + \frac{1}{6}\left(4g_1^* + g_5^* + g_8^*\right)$$
$$P_7^{*,g}(\boldsymbol{g}^*) = g_7^* + \frac{1}{6}\left(4g_1^* + g_5^* + g_8^*\right)$$

- $\forall \boldsymbol{x} \in \partial\mathcal{D}_{\mathrm{out}}$:

$$P_1^{*,f}(\boldsymbol{f}^*, \boldsymbol{g}^*, \boldsymbol{f}, \boldsymbol{g}) = f_1^* - f_3^* + \frac{1}{3}\left(4f_3^* + f_6^* + f_7^*\right) + \frac{1}{6}\left(\frac{\zeta}{1+3\eta}\right)\left(4g_3^* + g_6^* + g_7^*\right) + \frac{c_A(\boldsymbol{g})}{|\partial\mathcal{D}_{\mathrm{out}}|} = 0$$
$$P_5^{*,f}(\boldsymbol{f}^*, \boldsymbol{g}^*, \boldsymbol{f}, \boldsymbol{g}) = f_5^* - f_7^* + \frac{1}{3}\left(4f_3^* + f_6^* + f_7^*\right) + \frac{1}{6}\left(\frac{\zeta}{1+3\eta}\right)\left(4g_3^* + g_6^* + g_7^*\right) + \frac{c_A(\boldsymbol{g})}{|\partial\mathcal{D}_{\mathrm{out}}|} = 0$$
$$P_8^{*,f}(\boldsymbol{f}^*, \boldsymbol{g}^*, \boldsymbol{f}, \boldsymbol{g}) = f_8^* - f_6^* + \frac{1}{3}\left(4f_3^* + f_6^* + f_7^*\right) + \frac{1}{6}\left(\frac{\zeta}{1+3\eta}\right)\left(4g_3^* + g_6^* + g_7^*\right) + \frac{c_A(\boldsymbol{g})}{|\partial\mathcal{D}_{\mathrm{out}}|} = 0$$
$$P_1^{*,g}(\boldsymbol{g}^*, \boldsymbol{f}) = g_1^* - \frac{1}{6}\left(\frac{1-3\eta}{1+3\eta}\right)\left(4g_3^* + g_6^* + g_7^*\right) + \frac{\eta}{|\partial\mathcal{D}_{\mathrm{out}}|}$$
$$P_5^{*,g}(\boldsymbol{g}^*, \boldsymbol{f}) = g_5^* - \frac{1}{6}\left(\frac{1-3\eta}{1+3\eta}\right)\left(4g_3^* + g_6^* + g_7^*\right) + \frac{\eta}{|\partial\mathcal{D}_{\mathrm{out}}|}$$
$$P_8^{*,g}(\boldsymbol{g}^*, \boldsymbol{f}) = g_8^* - \frac{1}{6}\left(\frac{1-3\eta}{1+3\eta}\right)\left(4g_3^* + g_6^* + g_7^*\right) + \frac{\eta}{|\partial\mathcal{D}_{\mathrm{out}}|}$$

- $\forall \boldsymbol{x} \in \partial\mathcal{D}_{\mathrm{ns}}$:

$$P^{*,f}_{(\boldsymbol{c}_i\cdot\boldsymbol{n}>0)}(\boldsymbol{f}^*) = f^*_{(\boldsymbol{c}_i\cdot\boldsymbol{n}>0)} - f^*_{(\boldsymbol{c}_{\bar{i}}\cdot\boldsymbol{n}<0)} = 0,$$
$$P^{*,g}_{(\boldsymbol{c}_i\cdot\boldsymbol{n}>0)}(\boldsymbol{g}^*) = g^*_{(\boldsymbol{c}_i\cdot\boldsymbol{n}>0)} - g^*_{(\boldsymbol{c}_{\bar{i}}\cdot\boldsymbol{n}<0)} = 0.$$

(39)

with:

$$
\begin{aligned}
&f_i^{*,\mathrm{eq}} = \textstyle\sum_{j=0}^{8} \frac{\partial f_j^{\mathrm{eq}}}{\partial f_i} f_j^*, \\
&Q_i^{*,f} = \textstyle\sum_{j=0}^{8} -g_j^* \left(\frac{3\,\omega_j\, c_A}{\tau_g} \right) \boldsymbol{c}_j \cdot \boldsymbol{c}_i, \\
&g_i^{eq,*} = \textstyle\sum_{j=0}^{8} \frac{\partial g_j^{eq}}{\partial g_i} g_j^*, \\
&Q^{*,g} = \textstyle\sum_{j=0}^{8} \frac{\partial s_j}{\partial g_i} g_j^*, \\
&\eta = -\rho_{\mathrm{out}} + f_0 + f_2 + f_4 + 2(f_1 + f_5 + f_8), \\
&\zeta = \tfrac{6(g_1+g_5+g_8)}{(1+3\eta)}.
\end{aligned}
\tag{40}
$$

To compute the different adjoint-state variables, the steady-state solution of the forward problem is used. The adjoint-states being computed, the cost function gradient is finally computed through

$$
\begin{aligned}
&\nabla_\Psi \widehat{\mathcal{J}}^+ \left(\boldsymbol{f}, \boldsymbol{g}, \boldsymbol{f}^*, \boldsymbol{g}^* \right) = \\
&\quad - \alpha'(\Psi) \int_0^{t_f} \sum_{i=0}^{8} \omega_i f_i^* \left(\mathbf{M}^{-1}\mathbf{S}\mathbf{M} \left(3\,\boldsymbol{c}_j \cdot \boldsymbol{u} + \frac{9}{2}(\boldsymbol{c}_j \cdot \boldsymbol{u})^2 - \frac{3}{2}\boldsymbol{u}^2 \right) \right)_i \mathrm{d}t \\
&\qquad\qquad - \alpha'(\Psi) \int_0^{t_f} \sum_{i=0}^{8} \frac{3\,\omega_i\, g_i^* c_A\, \boldsymbol{c}_i \cdot \boldsymbol{u}}{\tau_g} \mathrm{d}t.
\end{aligned}
\tag{41}
$$

The general topology optimization algorithm is detailed in Algorithm 1. The iterative algorithm involves a criterion based on the stabilization of the cost function value which is detailed in the next section.

Algorithm 1: General topology optimization algorithm

Input: Level-set function $\Psi^{(0)}$;

Topology $\mathcal{T}^{(0)}$ through $\alpha^{(0)}$ (see eq. (10)), along with the smooth version eq. (12) ;

while *criterion* (43) *not satisfied* **do**

- Compute the Boltzmann variables $\boldsymbol{f}$ and $\boldsymbol{g}$ solving eq. (31);
- Compute the cost function value $\widehat{\mathcal{J}}^{+}(\boldsymbol{f}, \boldsymbol{g})$ with eq. (35);
- Compute the adjoint Boltzmann variables $\boldsymbol{f}^{*}$ and $\boldsymbol{g}^{*}$ solving eq. (39);
- Compute the cost function gradient $\nabla_{\Psi}\widehat{\mathcal{J}}^{+}$ from eq. (41);
- Update of the geometry : actualization of the level-set function with eq. (9);

return *Optimal topology* $\mathcal{T}^{(*)}$*;*

5. Test cases and results

For the validation of the proposed method, the reader is referred to a previous work of the authors [15] where a thermal fluid flow topology optimization case has been computed by following a similar procedure. The obtained results have been then compared with a benchmark test in literature and a study about the grid independency and the sensitivity of the algorithm to different initializations have also been conducted.

The geometry and the configuration of the test cases are shown on fig. 1. The 2D square domain is enclosed by no-slip walls. The gray layers, shown on fig. 1, represent the fixed solid boundary, on which the no-slip condition is applied. The cavity contains the fluid-solid distribution, and the set of inlet/outlet is also schematically represented. At the inlet, $\partial\mathcal{D}_{\text{in}}$, the fluid enters with a parabolic velocity profile.

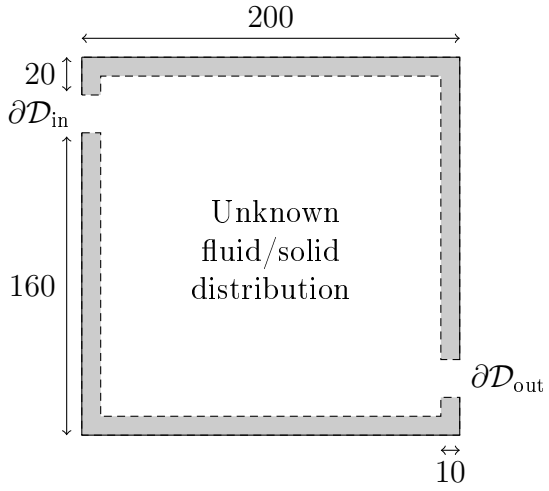

Figure 1: Schematic representation of the optimization problem configuration.

The convergence criterion for both the forward LBM problem and the adjoint-state LBM problem has been chosen to be:

$$\frac{\left|\left|a^{(n)} - a^{(n-10{,}000)}\right|\right|_{\infty}}{\left|\left|a^{(n-10{,}000)}\right|\right|_{\infty}} < 10^{-4} \quad \text{with} \quad \left|\left|a^{(n)}\right|\right|_{\infty} = \max_{\substack{q=\{f,g\} \\ j=0,\ldots,8 \\ i=1,\ldots,N}} \left|q_j^{(n)}(x_i)\right|, \tag{42}$$

in which the infinity norm is applied on the vector involving all the nine directions, and all spatial nodes, for both quantities, and the superscript (n) stands for the LBM iteration count. Besides, the convergence criterion of the optimization problem is based on the stabilization of the cost function value along with ten successive iterations:

$$\left| \frac{\mathcal{J}^{(k)} - \mathcal{J}^{(k-10)}}{\mathcal{J}^{(k-10)}} \right| < 10^{-4}, \tag{43}$$

where $\mathcal{J}^{(k)}$ is the cost function value at the iteration count k. Calculations were performed on a NVIDIA Quadro K6000 GPU card for taking advantage of the LBM algorithm parallelism. Normally, for the adjoint-states calculation, one needs to store the macroscopic values of the forward problem, at each LBM iteration, which is prohibitive in terms of memory requirement. Only steady-state problems are considered here, so, as stated by [29], the solution of the forward problem at final time can be used as the stationary source term for the whole adjoint-states calculation.

Regarding the reaction source term, instead of the simple linear model introduced previously in the adimensionnalised Damkohler number, a two-parameters model is chosen for a more tunable reaction:

$$s = k\left(1 - \exp(-rc_A)\right), \tag{44}$$

The coefficient k controls the maximum reaction rate, and r is a positive user-defined parameter that controls the dependency to the concentration: a high value prescribes a quasi-independent concentration rate whereas a small value tends to a linear model.

The numerical examples presented in this section use the following parameters:

- the spatial discretization for the domain is 200×200 elements,
- the reaction rate coefficient k is equal to 2×10^{-5},
- the Peclet number Pe is 2000,
- the initialization starts with the full fluid topology, i.e. with $\Psi(\boldsymbol{x}) > 0$,
- the iteration matrix $\mathbf{P}$ used for the level-set function evolution in eq. (9) is chosen to be a diagonal matrix satisfying $\mathbf{P}_i = {}^{0.01}/_{\alpha'(\Psi_i)}$. The benefit

of this choice is threefold: i) the derivative $\alpha'(\Psi) \geq 0$ is no longer involved in the level-set function evolution, so even a discontinuous function $\alpha(\Psi)$ can be used; ii) the user-parameter ϵ is not to be pre-assigned to a given value, this parameter being no longer involved anywhere in the optimization process; iii) there is no more bias between the response of the forward model, i.e. the value of the cost function $\mathcal{J}$ which would need $\epsilon = 0$, and its gradient, $\nabla_\Psi \mathcal{J}$, which would need $\epsilon \neq 0$ for its existence condition. Next, the descent parameter 0.01 involved at the numerator of the iteration matrix, has been chosen following Dugast et al. [15].

- the maximal allowed pressure drop is twice the initial pressure drop (calculated at the first iteration with the full fluid geometry),
- the relaxation times for the MRT are set to $s_e = s_\epsilon = s_q = 0.6$ and $s_\nu = 1/(3\nu + 0.5)$.
- the reaction rate coefficient r is equal to 10, which corresponds to a Damkholer number Da equal to 0.1.

As the MRT model allows the calculation of higher Reynolds number flows compared to the SRT model, the first study described hereafter is based on the influence of the Reynolds number on the optimized topology. Three cases are presented : Re =10, Re =100 and Re =1000. It is to be noticed that although the forward and adjoint-state problems could have been solved with the single-relaxation time model, for both Re=10 and Re=100, the convergence of the LBM solver is not possible without a modification of the relaxation times s_{0-6} for Re =1000. This study shows that the introduction of the solid parts breaks the main fluid flow path going from the inlet to the outlet via the center of the domain into several fluid paths. This is true for the three tested Reynolds numbers. This path division participates to a better distribution of the fluid flow on the entire domain, especially on the top-right and bottom-left corners compared to the initial configuration. One can notice that the complexity of the flow paths increases with the Reynolds number. Apart from advection, the forward problem involves also diffusion and reaction phenomena. Consequently, the second study deals with the influence of the mass diffusivity and of the reaction rate on the obtained topology. The modification of the mass diffusivity affects the balance between advection and diffusion and therefore the impact of the fluid flow velocity on

the concentration. The reaction rate is used to control the speed on the reaction. The influence of a faster reaction will be studied. With these two studies, the topology optimization method has been tested for different flow regimes and reactants. It shows its ability to produce specific optimized topologies for a variety of configurations.

5.1. Influence of the Reynolds number

The first study deals with the influence of the Reynolds number on the obtained optimized topology. The objective is the maximization of the reaction within the domain, this measurement being calculated at the outlet, see eq. (35). For this study, the Peclet number is kept constant. As $\mathrm{Pe} = \mathrm{Re} \times \mathrm{Sc}$, it means that the Schmidt number is also modified along with the Reynolds number.

5.1.1. Case 1 : Re =10

Figure 2 presents the results of the optimization process along with the iterations, for the first case, with Re =10. On the top and left-hand side is presented the evolution of both the cost function value (mean of $u \times c_{\mathrm{out}}$), and of the pressure drop ratio $\frac{\Delta p}{\Delta p_{\max}}$, along with the iteration count. On the right-hand side, is presented the evolution of the topology: $\mathcal{T}^{(0)}_{[\mathrm{Re}=10]}$ at the iteration 0 (it is the initial guess), $\mathcal{T}^{(30)}_{[\mathrm{Re}=10]}$ at the iteration 30, $\mathcal{T}^{(50)}_{[\mathrm{Re}=10]}$ at the iteration 50, and after reaching the stabilization of the cost function value, $\mathcal{T}^{*}_{[\mathrm{Re}=10]}$, at the iteration 900.

From this figure it is seen that the solid parts are introduced only in the center of the domain, but not close to both the inlet and the outlet. That is the reason why the increase in the pressure drop ratio is not much, and the constraint on the pressure drop is by far fulfilled. In fact, the introduction of the solid medium close to the center of the medium divides the flow in two distinct paths, as can be seen from fig. 2, in the middle. This makes such that the fluid velocity is greater elsewhere, especially close to the bottom right and top left corners. The effect is that more reactant is consumed in these areas; this participates to the high decrease of the outlet concentration (see the bottom of fig. 2). Note that, from the initial guess to the optimized topology, the cost function has decreased from 5.10^{-3} (LB unit) down to $1.96.10^{-3}$ (LB unit), i.e. by a factor more than 2.5.

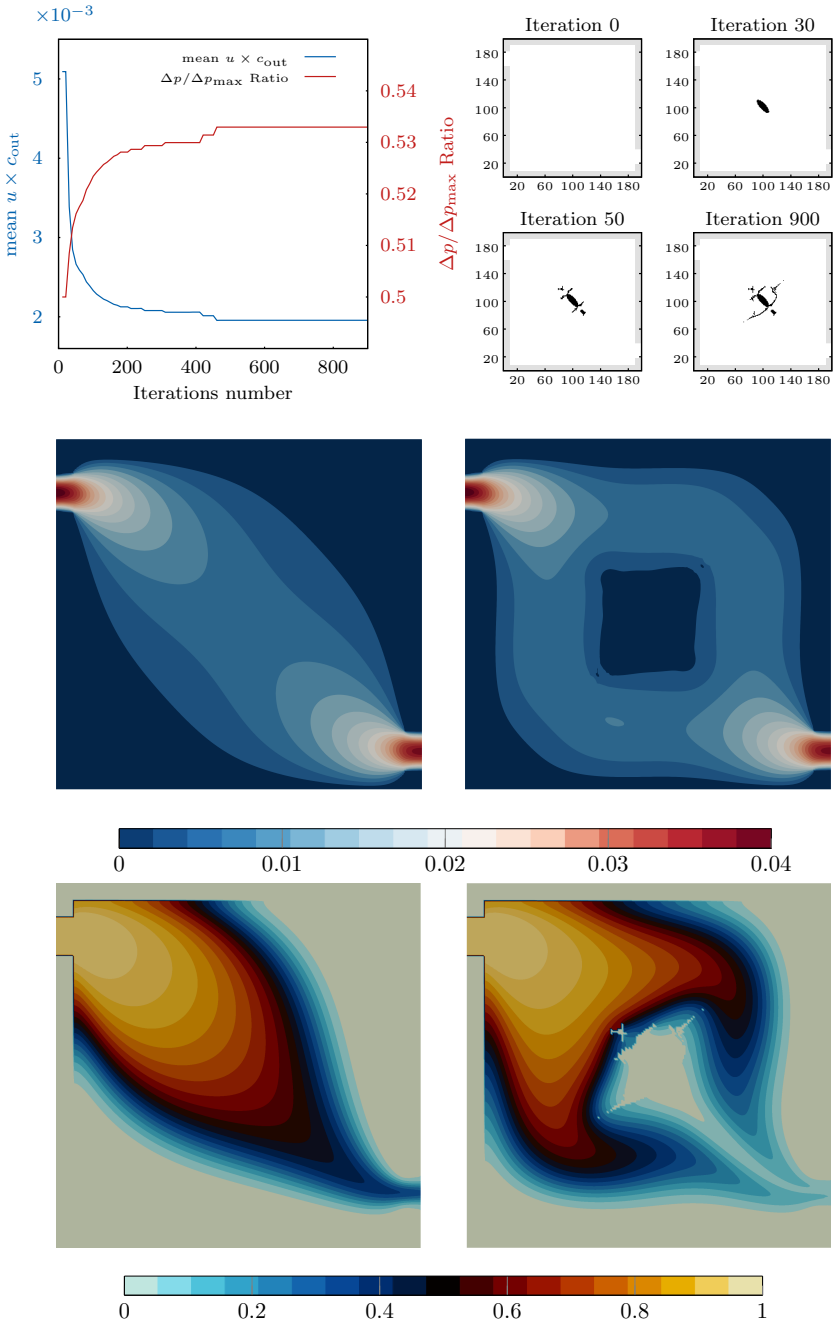

Figure 2: Re=10. Top left: evolution of the cost function and of the pressure drop ratio along with the iteration count. Top right: the topology at iterations 0, 30, 50, and 900. Middle: module of the velocity field. Left: guess configuration (full fluid). Right: optimized topology. Bottom: concentration field. Left: guess configuration (full fluid). Right: optimized topology.

5.1.2. Case 2 : Re =100

Figure 3 presents the results of the optimization process along with the iterations, for the second case, with Re =100. On the top and left-hand side is presented the evolution of both the cost function value (mean of $u \times c_{\text{out}}$), and of the pressure drop ratio $\frac{\Delta p}{\Delta p_{\max}}$, along with the iteration count. On the right-hand side, is presented the evolution of the topology: $\mathcal{T}^{(0)}_{[\text{Re}=100]}$ at the iteration 0 (it is the initial guess), $\mathcal{T}^{(20)}_{[\text{Re}=100]}$ at the iteration 20, $\mathcal{T}^{(50)}_{[\text{Re}=100]}$ at the iteration 50, and after reaching the stabilization of the cost function value, $\mathcal{T}^{*}_{[\text{Re}=100]}$, at the iteration 390. Comparing fig. 3 with fig. 2, it can be seen that the decrease of the cost function is more important for Re=100 than for Re=10. Here, the cost function has decreased from $6.1.10^{-3}$ (LB unit) down to $5.96.10^{-4}$ (LB unit), i.e. by a factor greater than 10 .

Conversely to the previous case with Re=10, the optimal fluid/solid configuration is here composed of several parts, located near the diagonal of the domain, facing the main fluid flow stream. The fluid flow is thus mainly directed towards the corners, but also a part of it goes through the center of the domain, as the solid line is not continuous, containing some holes, see the plot in the middle of fig. 3.

The outlet concentration for the optimized geometry is very close to zero, as can be seen from the plot in the bottom of fig. 3. This means that almost all the reactant has been consumed inside the domain. In that sense, the efficiency of the chemical reaction has been highly increased.

5.1.3. Case 3 : Re =1000

In this last test case about the Reynolds number study, the velocity and concentration fields for Re = 1000 are radically different to previous cases, with Re = 10 and Re = 100. As a matter of fact, the fig. 4 is to be compared to fig. 2 and fig. 3, middle and left-hand side for the velocity, and bottom and left-hand side for the concentration, at the initial guess, i.e. for the full fluid flow case. In fact, when Re = 1000, a re-circulation zone appears around the center of the domain. As a consequence, the concentration is very small there at the center of the vortex, but the concentration remains very high at the outlet.

The fluid/solid configuration found by the implemented topology optimization algorithm is, indeed, very far away from an optimized one, as the optimization process is struggling to find any proper topology. In order to facilitate the convergence of the optimization problem, the initial configura-

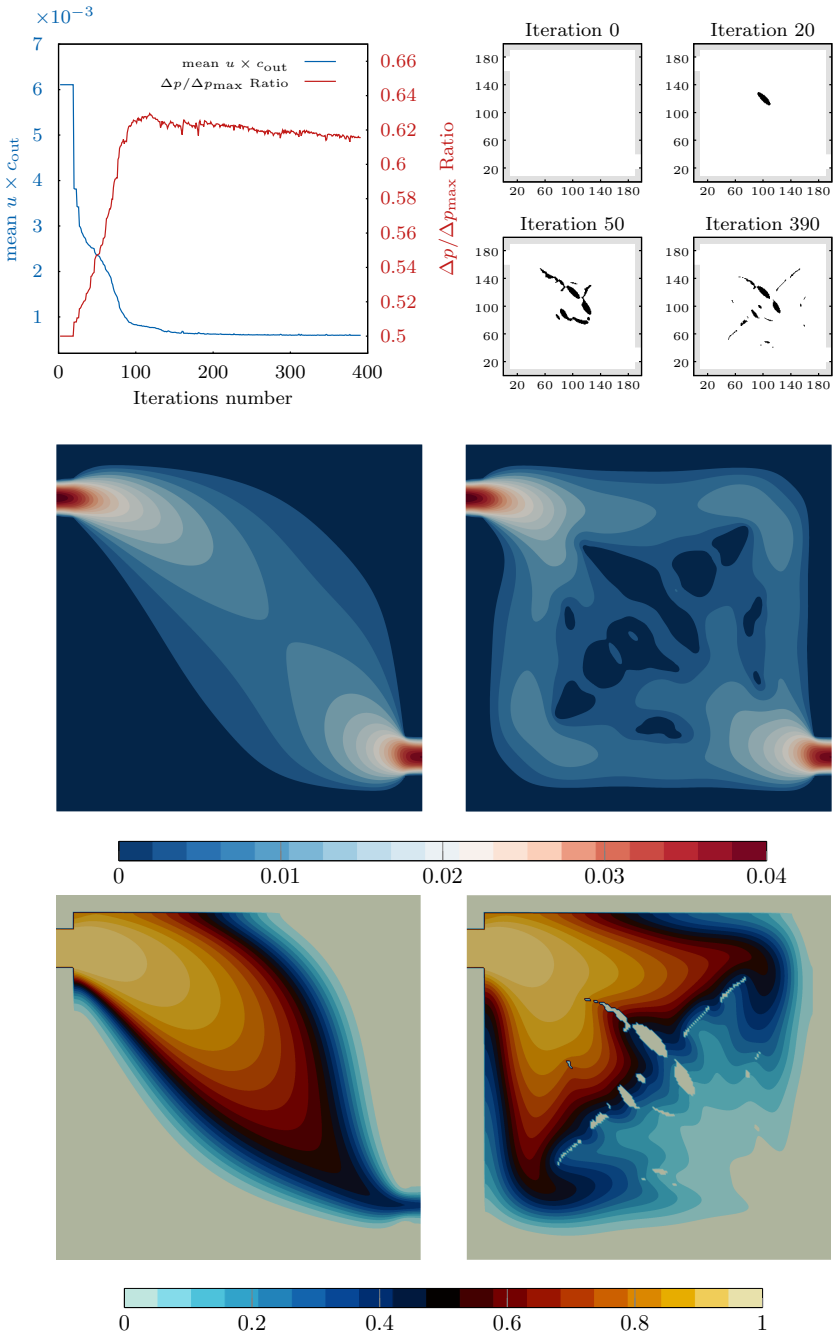

Figure 3: Re=100. Top left: evolution of the cost function and of the pressure drop ratio along with the iteration count. Top right: the topology at iterations 0, 20, 50, and 390. Middle: module of the velocity field. Left: guess configuration (full fluid). Right: optimized topology. Bottom: concentration field. Left: guess configuration (full fluid). Right: optimized topology.

tion was set to a uniform distribution of small solid circles inside the domain. With such an initialization, the re-circulation disappears, and the research of optimized geometries is easier. Note that the cost function value for the full fluid geometry was $12.6.10^{-3}$ (LB unit) while it is now $4.5.10^{-3}$ (LB unit) with this initialization, i.e. with circles.

The evolution along with the optimization iterations of the cost function and of the pressure drop limitation are shown on fig. 5, for this case. At the beginning of the optimization process, the pressure drop increases. This is due to the fact that some solid parts are introduced at the outlet of the domain. This may be seen as a drawback, but in fact, this also participates to the decrease of the concentration field at the outlet, which is the main objective of the optimization problem. Then, after some iterations, the limitation of the pressure drop included in the augmented cost function helps to prevent from the introduction of more solid parts near this area. The different solid parts introduced inside the domain are found to be very small: it is even difficult to see the difference between the different optimization steps, without a close look. But these small modifications have a huge impact on the cost function decrease.

As can be seen on fig. 5, a fluid path has been drawn on the left-hand side of the domain, by removing some solid elements from the initial topology. The distribution of the reactant is then more uniform, and the reaction rate is more important in this area, which participates to a diminution of the outlet concentration, as can be seen on the plot on the bottom of fig. 5. In that case again, the efficiency of the chemical reaction has been highly increased.

5.1.4. Crosscheck of the different optimized configurations

Based on the Reynolds number test cases, a crosscheck comparison of the different optimal topologies has been performed in order to discuss on the results. In this additional study, the fluid flow with Reynolds numbers equal to 10, 100, and 1000 is applied on the three previously obtained optimal topologies. The cost function measuring the reaction efficiency is then calculated for each of these nine cases. The results are reported in table 1. The first row is related to the three different found optimal topologies, and the first column is related to the Reynolds number which is applied. The other numbers are the values of the calculated cost function.

The expected result is that the minimum value of the cost function is to be found for the applied Reynolds number equal to the one related to its optimal geometry. For readability considerations, the minimum value of

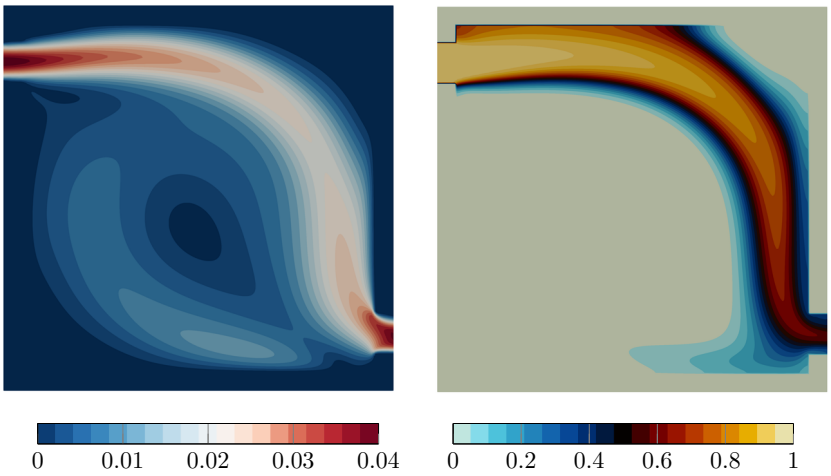

Figure 4: Re=1000. Velocity (left) and concentration (right) fields for the full fluid topology.

	$\mathcal{T}^*_{[\mathrm{Re}=10]}$	$\mathcal{T}^*_{[\mathrm{Re}=100]}$	$\mathcal{T}^*_{[\mathrm{Re}=1000]}$
Re =10	1.9	**0.8**	2.6
Re =100	2.3	**0.59**	2.6
Re =1000	12.6	8.4	**0.49**

Table 1: Cost function values ($\times 10^{-3}$) for different configurations

the cost function for each Reynolds number is written in bold characters, in table 1.

For the applied Reynolds number equal to 100, one can see that the related optimized topology, $\mathcal{T}^*_{[\mathrm{Re}=100]}$, provides, by far, the best result. The same trend is observed for the applied Reynolds number equal to 1000, but with even a higher difference between the three topologies: the cost function is equal to 0.49 with the topology $\mathcal{T}^*_{[\mathrm{Re}=1000]}$, while it is equal to 8.4 and 12.6, for topologies $\mathcal{T}^*_{[\mathrm{Re}=100]}$ and $\mathcal{T}^*_{[\mathrm{Re}=10]}$, respectively.

However, for the applied Reynolds number equal to 10, it is seen from table 1 that the minimum cost function value is given for the topology $\mathcal{T}^*_{[\mathrm{Re}=100]}$. This highlights that the topology obtained at the end of the optimization process, after convergence, for the case of Re = 10, is a local minimum. Even if this crosscheck did not show a local minimum for the two other configurations, it is to be noticed that this does not mean that the global minimum

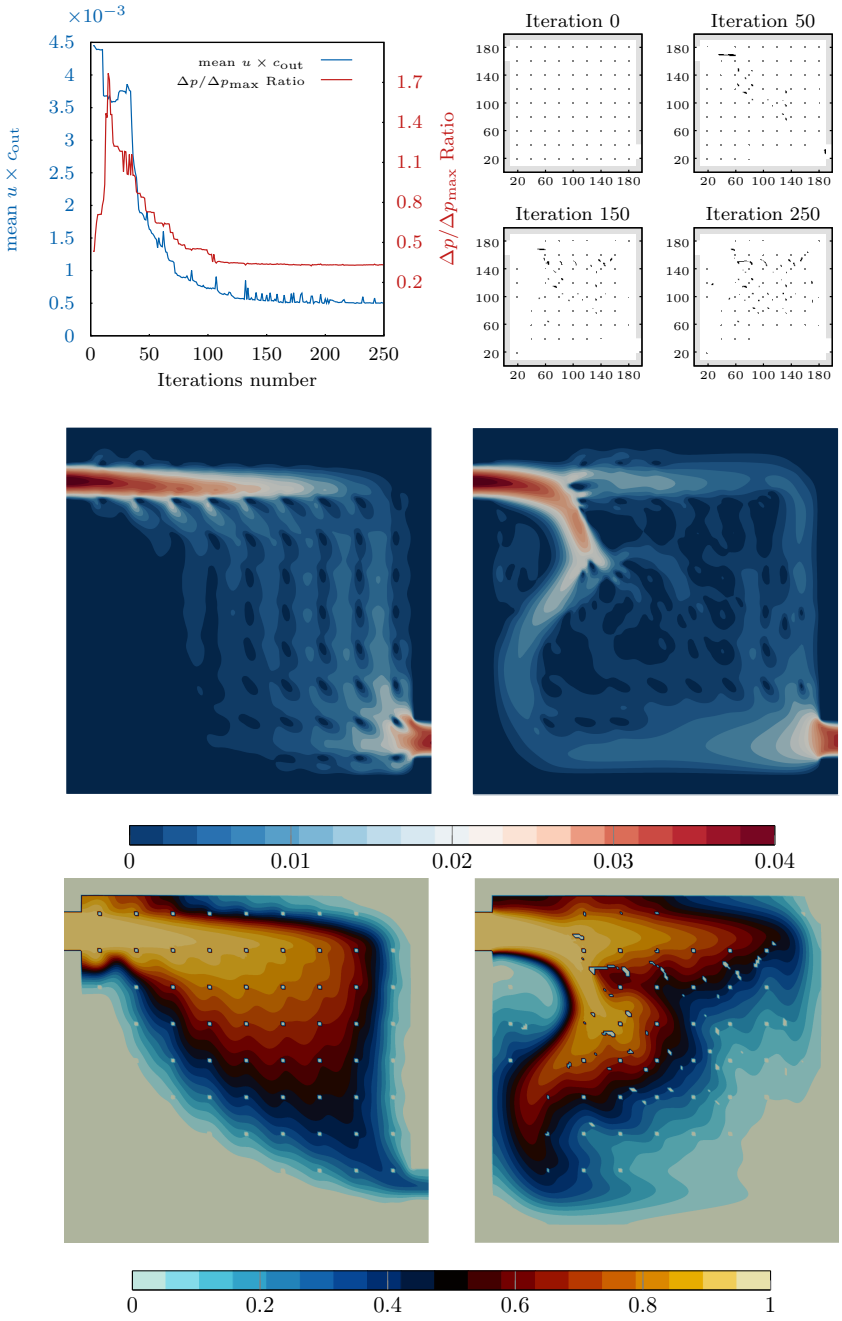

Figure 5: Re=1000. Top left: evolution of the cost function and of the pressure drop ratio along with the iteration count. Top right: the topology at iterations 0, 50, 150, and 250. Middle: module of the velocity field. Left: guess configuration. Right: optimized topology. Bottom: concentration field. Left: guess configuration. Right: optimized topology.

has been actually reached. In fact, it is well known that gradient-type methods, because they are based on a local study of the function to be minimized, usually reach a local minimum next to the initial guess [66]. This is usually considered as the main drawback of these gradient-type algorithms. But, at the same time, compared to gradient-free optimization methods – which, indeed, are more likely to find the global minimum, gradient-type algorithms reach the minima much more efficiently. This point makes the difference. In fact, the optimization problem treated here involves 200×200 unknowns; such a discretization would be impracticable with any gradient-free optimizer. This difficulty could of course be overcome by modifying the initial topology, many times, but, as the physical problem is complex, it will remain difficult (and likely impossible) to find the unique global minimum.

In further perspectives, the local minimum treatment is an interesting issue to solve, despite the fact that it can be difficult to avoid them while using a gradient-based optimization method. Nevertheless, one possibility would be to use a multi-scale resolution approach. Such a multi-resolution approach, formalized by Liu [67] for solving some ill-posed inverse problems, has been later on successfully used by Dubot et al. [68] and Liu [69], for example. In the framework of reactive fluid flow topology optimization, the use of a multi-scale resolution approach would enable to perform a scale-by-scale optimization on successive convex cost functions, following the work of Chavent [70]. Moreover, added to this interesting property, this would also save computational time due to faster convergence. This point will be addressed in a future research.

Following the study of the Reynolds number, the influence of both the reaction rate and diffusion is investigated. Additionally, the Damkholer and Peclet number are modified to determine their effect on the resultant system geometry.

5.2. Case 4 : Influence of the Damkohler number

The reaction rate k is now modified in order to evaluate the influence of the Damkohler number on the optimal topology. It has been increased from 2×10^{-5} to 4×10^{-5}. Though this modification does not have any impact on the velocity, the concentration field is altered, as the reactant is consumed faster. This effect is clearly visible by comparing figs. 5 and 6.

Concerning the optimization results, one can observe a similar trend between this case and the previous case 3. First, the evolution of the cost function and the pressure drop ratio, represented on the top of fig. 6, are

similar: one observes an increase and then a decrease of the pressure drop ratio, while the outlet concentration is decreasing. The optimal topology is also comparable to the one of case 3: it implies the same modification on the velocity in which the flow is divided into two main streams just after the inlet. The main difference between both the previous case 3 and this case 4 is in the magnitude of the outlet concentration. This one is much smaller for the higher Damkholer number, as it was expected.

One can also see from fig. 7 (left) that the solid part at the core of the domain is denser for Da=0.1 (in red) than for Da=0.2 (in blue). Please note that, to enhance readability, the solid parts have been represented larger (in this figure only). For Da=0.2, because the reactant is consumed faster (with respect to Da=0.1), it is consequently easier to obtain a small concentration at the outlet, even without the need to alter the velocity field through the addition of significant solid material. The comparison of the concentration field for the two Damkholer numbers is shown on fig. 7 (right). The threshold $c_A \gtrless 0.05$ is applied to the concentration field to get a better contrast between the two cases. For the higher Damkholer number, one can see that the concentration becomes very low shortly after the middle of the domain. As the reactant has been almost entirely consumed, the efficiency has been highly increased regarding to the cost function. However, the other conclusion that can be made based on this result is that the reactor has been over-sized for this reaction rate. In fact, based on the concentration field obtained for the optimized geometry, one can conclude that a good efficiency could have also been achieved with a smaller reactor. The real cost of the chemical reactor and the dimensions associated with it were not included in the optimization problem; it is nevertheless a useful conclusion from an engineering point of view.

5.3. Case 5 : Influence of the Peclet number

In the previous numerical examples, the Peclet number was equal to 2000. The advection process played a major role compared to the diffusion process. In this test case 5, the Peclet number is modified to be equal to 100. For the rest, the configuration is kept the same as for the previous case 3, and the Reynolds number is 1000. Note that in this case, the diffusion process is no longer negligible in the chemical reaction. Concerning the forward problem, the velocity field is not altered by this modification. However, important changes are observed in the concentration field. The pressure drop ratio is important for this case, as can be seen from fig. 8, on the top left. This

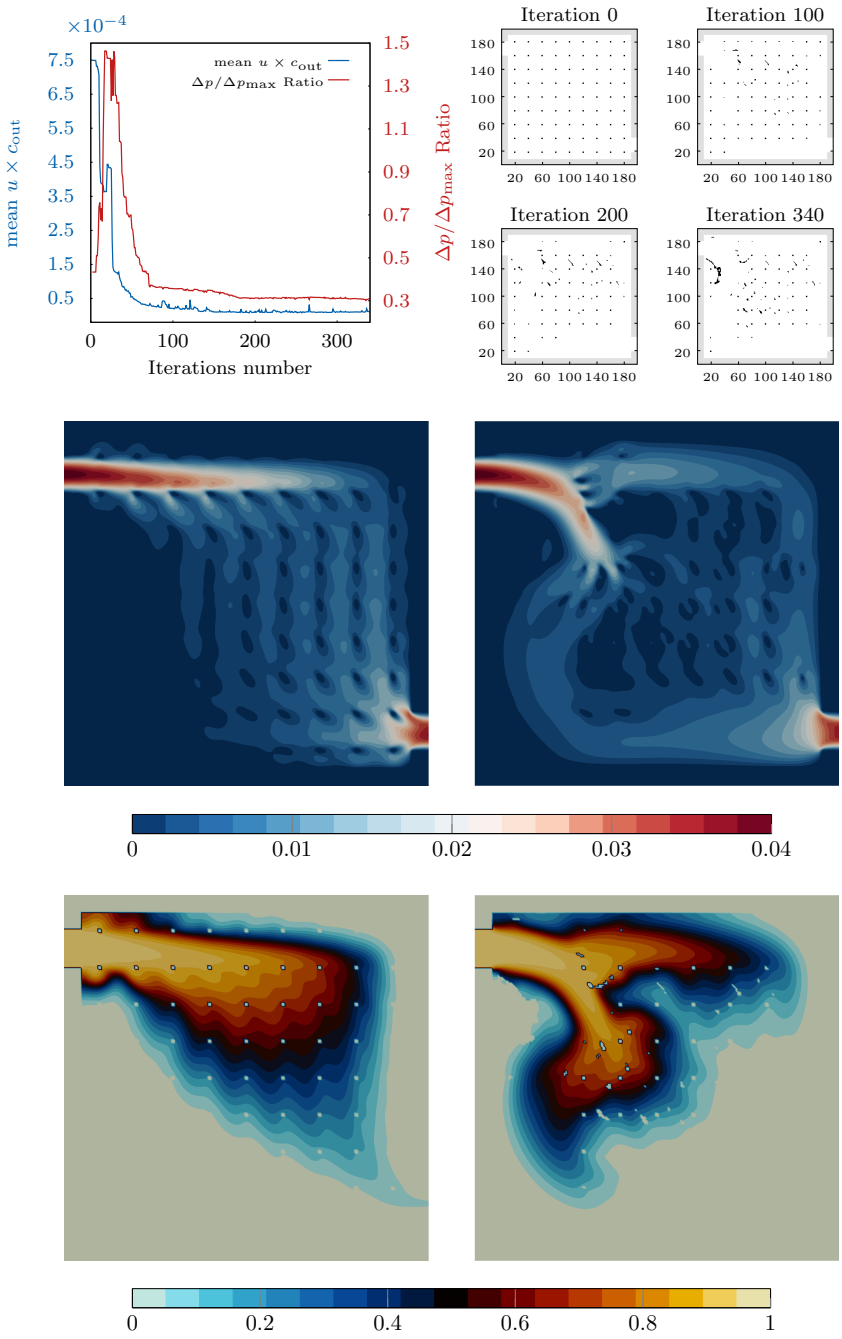

Figure 6: $\mathrm{Da} = 4 \times 10^{-5}$. Top left: evolution of the cost function and of the pressure drop ratio along with the iteration count. Top right: the topology at iterations 0, 100, 200, and 340. Middle: module of the velocity field. Left: guess configuration (full fluid). Right: optimized topology. Bottom: concentration field. Left: guess configuration (full fluid). Right: optimized topology.

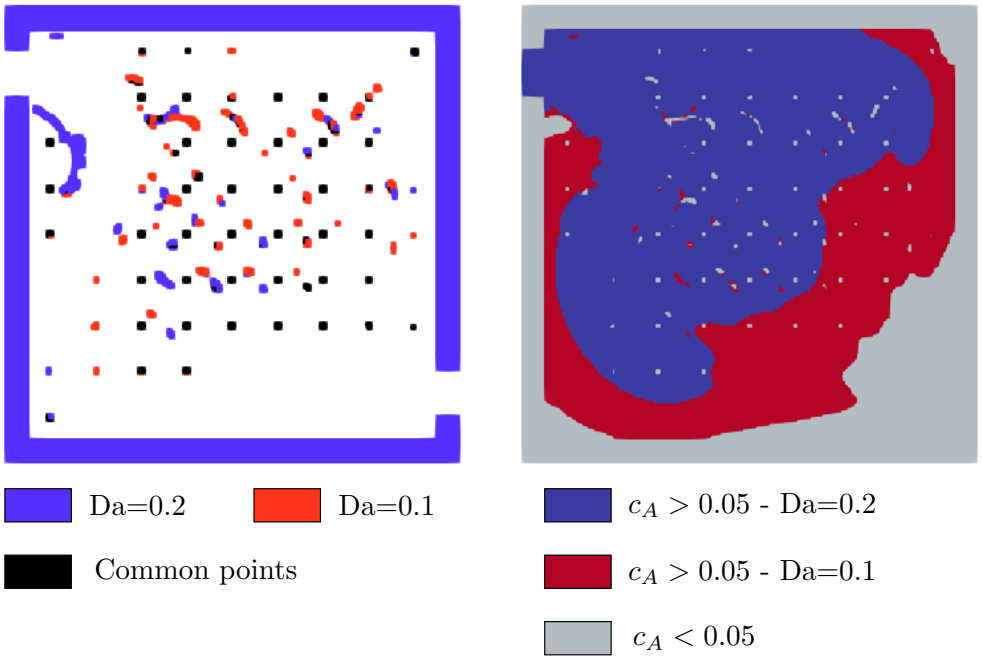

Figure 7: Comparison of optimization cases for Da=0.1 and Da=0.2: optimal topologies (left) and concentration levels (right)

can be explained by the presence of solid parts near both the inlet and the outlet of the domain. Similarly to previous examples, the flow is divided into two paths near the inlet. With the initial topology, the reactant was spread from the inlet towards only the top-right corner of the domain. With the optimal topology, an equilibrium has been found between the propagation of the reactant on both the top-right corner and the bottom-left corner: a symmetry of the concentration can be observed, from the inlet down to the outlet. One can notice that, to obtain this behavior, the fluid flow is progressively divided into smaller channels from the inlet to the center of the domain. Indeed, the density of solid parts is the most important on the diagonal connecting the bottom-left corner to the top-right corner. With such a pattern, the minimization of the outlet concentration is well achieved.

5.4. Overview and analysis of the different results

The characteristics of the optimized geometries obtained for all cases are summarized in table 2.

Among all cases, the decrease of the cost function is less important for Re=10 (case 1) and for Pe=100 (case 5). In these two cases, either the advection is the smallest (Re=10, case 1), or the diffusion is the greatest (Pe=100, case 5), and the consequences are the same: the impact of the velocity field on the concentration is reduced, and so is the impact of the topology on the chemical reaction efficiency.

For the study on the Damkholer number, the reaction rate is multiplied by 2 (from the test case 3 to the test case 4), and the impact of this modification is consequent on the final value of the cost function. The initial value was also lower than the other cases, about one order of magnitude compared to the case 3. As it has been stated in section 5.2, the major conclusion regarding the optimized geometry obtained for this case is not only the efficiency of the reaction, but rather the over-sizing of the reactor. In fig. 7, one can see that there are less solid parts in the core of the domain for Da =0.2 than for Da =0.1. The porosity value in table 2 does not reflect this, but this can be explained by the fact that for Da =0.2, the biggest solid part (which is curved and close to the inlet) represents alone 0.37 % of the total porosity.

From table 2, it is seen that the pressure drop ratio slightly increases for Re=10 (case 1) and for Re=100 (case 2), but this pressure drop decreases for Re=1000 (case 3) and Da=0.2 (case 4). In all cases, as the maximal pressure drop is prescribed to twice the pressure drop given for the initial geometry, the initial pressure drop ratio is equal to 0.5. So, for the two first

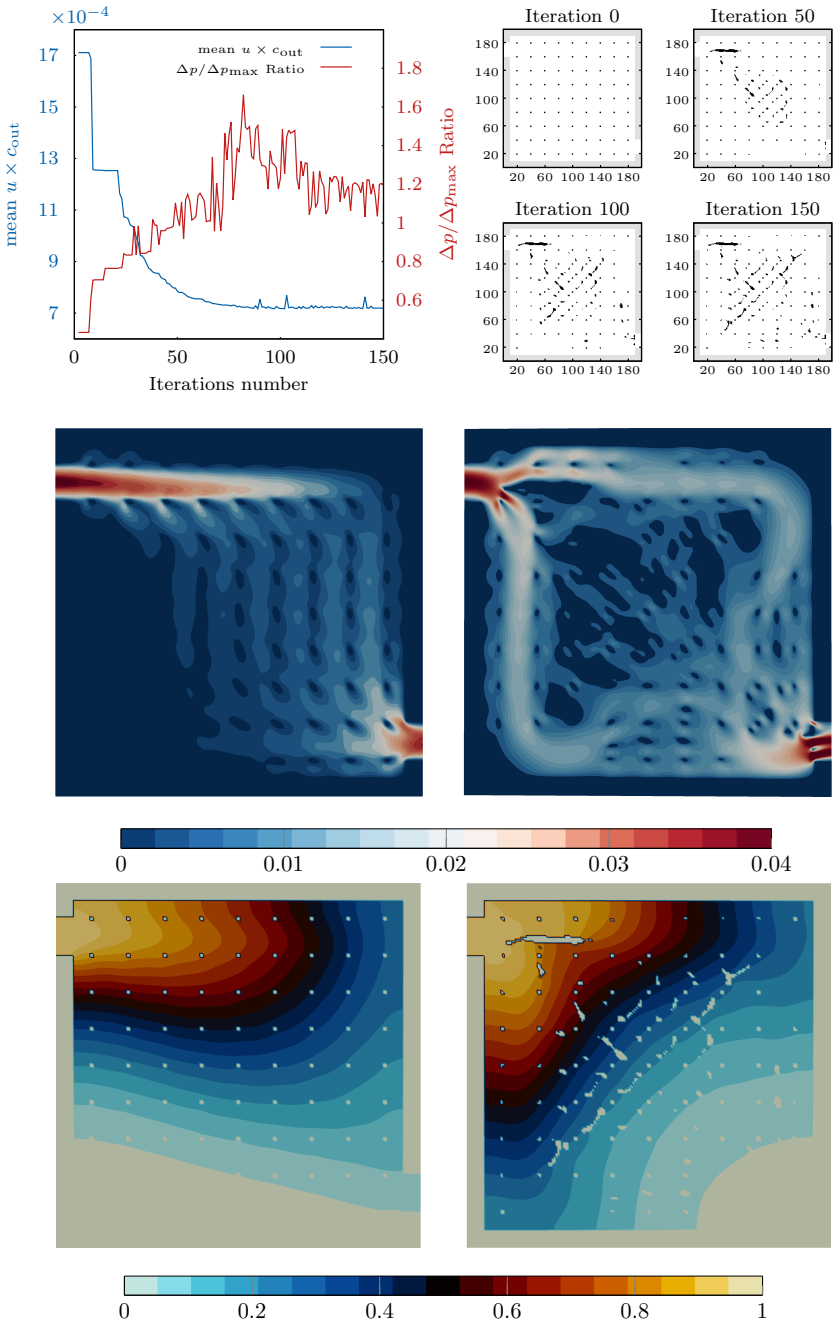

Figure 8: Pe=100. Top left: evolution of the cost function and of the pressure drop ratio along with the iteration count. Top right: the topology at iterations 0, 50, 100, and 150. Middle: module of the velocity field. Left: guess configuration (full fluid). Right: optimized topology. Bottom: concentration field. Left: guess configuration (full fluid). Right: optimized topology.

cases, any added solid within the void medium would increase this pressure drop ratio. However, as the initialization for Re=1000 is realized with a uniform distribution of small circles, the pressure drop can be smaller to the initial one if some circles are removed, especially near the inlet and near the outlet of the domain. This phenomenon happens for Re=1000 (case 3) and for Da=0.2 (case 4). For the test case 5 (study on the Peclet number), the initialization also involves circles, but, as some additional solid parts are introduced, especially near the inlet and near the outlet, this participates to an increase of the pressure drop ratio. As it can be seen on the different figures concerning this study, the porosity for a lower Peclet number is higher than for the other cases. The optimization domain is composed of more solid parts to have a stronger control on the velocity field, useful to counter-balance the higher diffusivity, but this is costly in term of pressure drop. One can notice that in all the cases, the optimization process is achieved by the addition of a small amount of materials (98.26 % of minimal final porosity, except for the low Pe number test). This last configuration is characterized by a lower porosity (97.1 %, which corresponds to three times more added material). The term porosity not only explains the amount of material but also its structure. Indeed, except at the lowest Re number, where optimal form acts as a profile by splitting the initial major flow, the optimal solid distributions look like porous media. In both the Re=100 case and low Pe number case, a plane structure appears in the diagonal of the cavity, perpendicular to the line joining the entrance and the exit. This structure acts as a perforated plane with adjusted holes in order to control and to balance the fluid flow.

In all these configurations, the optimization algorithm has been able to design different topologies able to increase the efficiency of the chemical reactors, showing its adaptability and usefulness working with several physical parameters involved in a multiphysics problem.

Case #	Da	Re	Pe	$\mathcal{J}^*$	$\mathcal{J}^{(0)}/\mathcal{J}^*$	Δp ratio	Porosity
1	0.1	10	2000	1.9	2.60	0.53	98.72%
2	0.1	100	2000	0.59	10.40	0.61	98.26%
3	0.1	1000	2000	0.49	9.08	0.33	98.85%
4	0.2	1000	2000	0.012	62.50	0.306	98.75%
5	0.1	1000	100	0.72	2.36	1.03	97.1%

Table 2: Optimization results for different configurations

6. Conclusion

A topology optimization algorithm has been developed for advection-diffusion-reaction equations. The physical goal was the maximization of the reaction within the porous domain. This was measured through the minimization of the concentration flow out of the domain. The evolution of the topology was performed thanks to the evolution of a level-set function and a gradient-type method. Both the forward and the adjoint-state problems have been computed with the lattice Boltzmann method, with a passive scalar approach, and a reaction term for the modeling of the concentration field. Though the single-relaxation time collision operator was used for the concentration field, the flow field has been conputed with the multi-relaxation time collision operator. This enabled computations with regimes up to Re=1,000. For both clarity and conciseness considerations, both forward and adjoint-state problems have been written down in residual forms.

The numerical applications enabled to exhibit strongly different behaviors with respect to the flow regime. Particularly, flows with Re=10, Re=100, and Re=1,000 have been tested. For the specific case of Re=1,000, it has been shown that the presence of the recirculation zone went against a good convergence of the optimization process. As such, a modification of the initial guess topology, with the introduction of different small solid zones inside the medium, leads to a better convergence of the optimization problem.

Then, a study of the most important physical parameters (Damkholer and Peclet numbers) involved in the chemical reaction was done. As this problem involves multiple coupled phenomena (advection, diffusion and reaction), their influence on the forward and optimization problem was important to be discussed. First, the reaction rate has been modified for the study on the Damkholer number. Even if the reactant was consumed faster, it was still possible for the algorithm to suggest an efficient design to minimize the cost function. Second, about the Peclet number, the choice was made for the first numerical examples to work with an advection-dominated problem, compared to mass diffusion, with a high Peclet number, in order for the velocity flow to have an important impact on the efficiency of the reaction. However, it was shown that the algorithm was also working fine with a lower Peclet number, where diffusion was not negligible anymore. In this case, a very regular symmetry has been achieved by the optimized fluid/solid distribution, participating to a substantial decrease of the outlet concentration.

A crosscheck has also been performed in order to evaluate the results,

and enhance the reliability of the topology optimization method. Although a local minimum was found for Re=10, the comparisons with Re=100 and Re=1000 has been successful as the best performance was achieved with the corresponding optimized geometry.

In further perspectives, the local minimum treatment is an interesting issue to solve, despite the fact that it can be difficult to avoid them while using a gradient-based optimization method. Nevertheless, one possibility would be to use a multi-scale resolution approach. Such a multi-resolution approach, formalized by Liu [67] for solving some ill-posed inverse problems, has been later on successfully used by Dubot et al. [68] and Liu [69], for example. In the framework of reactive fluid flow topology optimization, the use of a multi-scale resolution approach would enable to perform a scale-by-scale optimization on successive convex cost functions, following the work of Chavent [70]. Moreover, added to this interesting property, this would also save computational time due to faster convergence. This point will be addressed in a future research.

Acknowledgments

The authors thank the French Ministry of Higher Education and Research for funding this research. The authors also sincerely thank the reviewers for their highly constructive and wise remarks that enabled us to improve drastically the quality of this paper.

References

[1] M. Messaggi, P. Canzi, R. Mereu, A. Baricci, F. Inzoli, A. Casalegno, M. Zago, Analysis of flow field design on vanadium redox flow battery performance: Development of 3D computational fluid dynamic model and experimental validation, Applied Energy 228 (July) (2018) 1057–1070 (2018). doi:10.1016/j.apenergy.2018.06.148.

[2] J. Houser, A. Pezeshki, J. T. Clement, D. Aaron, M. M. Mench, Architecture for improved mass transport and system performance in redox flow batteries, Journal of Power Sources 351 (8) (2017) 96–105 (may 2017). doi:10.1016/j.jpowsour.2017.03.083.
URL http://dx.doi.org/10.1016/j.jpowsour.2017.03.083
https://linkinghub.elsevier.com/retrieve/pii/S0378775317303816

[3] R. Cervantes-Alcalá, M. Miranda-Hernández, Flow distribution and mass transport analysis in cell geometries for redox flow batteries through computational fluid dynamics, Journal of Applied Electrochemistry 0 (0) (2018) 0 (2018). doi:10.1007/s10800-018-1246-7.
URL http://dx.doi.org/10.1007/s10800-018-1246-7

[4] O. Sigmund, K. Maute, Topology optimization approaches, Structural and Multidisciplinary Optimization 48 (2013) 1031–1055 (2013). doi:10.1007/s00158-013-0978-6.
URL http://link.springer.com/10.1007/s00158-013-0978-6

[5] M. P. Bendsøe, Optimal shape design as a material distribution problem, Structural Optimization 1 (4) (1989) 193–202 (dec 1989). doi:10.1007/BF01650949.
URL http://link.springer.com/10.1007/BF01650949

[6] O. Sigmund, J. Petersson, Numerical instabilities in topology optimization: A survey on procedures dealing with checkerboards, mesh-dependencies and local minima, Structural Optimization 16 (1) (1998)

874 68–75 (aug 1998). doi:10.1007/BF01214002.
875 URL http://link.springer.com/10.1007/BF01214002

876 [7] T. Borrvall, J. Petersson, Topology optimization of fluids in Stokes flow,
877 International Journal for Numerical Methods in Fluids 41 (2003) 77–107
878 (2003). doi:10.1002/fld.426.

879 [8] A. Gersborg-Hansen, O. Sigmund, R. Haber, Topology optimization of
880 channel flow problems, Structural and Multidisciplinary Optimization
881 30 (3) (2005) 181–192 (sep 2005). doi:10.1007/s00158-004-0508-7.
882 URL http://link.springer.com/10.1007/s00158-004-0508-7

883 [9] G. Pingen, M. Waidmann, A. Evgrafov, K. Maute, A parametric level-
884 set approach for topology optimization of flow domains, Structural
885 and Multidisciplinary Optimization 41 (1) (2009) 117–131 (jun 2009).
886 doi:10.1007/s00158-009-0405-1.
887 URL http://link.springer.com/10.1007/s00158-009-0405-1

888 [10] V. J. Challis, J. K. Guest, Level set topology optimization of fluids in
889 Stokes flow, International Journal for Numerical Methods in Engineering
890 79 (10) (2009) 1284–1308 (sep 2009). doi:10.1002/nme.2616.
891 URL http://doi.wiley.com/10.1002/nme.2616

892 [11] G. Marck, M. Nemer, J. Harion, Topology Optimization of
893 Heat and Mass Transfer Problems: Laminar Flow, Numerical
894 Heat Transfer, Part B: Fundamentals 63 (2013) 508–539 (2013).
895 doi:10.1080/10407790.2013.772001.
896 URL http://www.tandfonline.com/doi/abs/10.1080/10407790.2013.772001

897 [12] E. Dede, Multiphysics topology optimization of heat transfer and fluid
898 flow systems, in: COMSOL Conference, 2009 (2009).
899 URL cds.comsol.com/access/dl/papers/6282/Dede.pdf

900 [13] J. Alexandersen, O. Sigmund, N. Aage, Large scale three-dimensional
901 topology optimisation of heat sinks cooled by natural convection, Inter-
902 national Journal of Heat and Mass Transfer 100 (2016) 876–891 (2016).
903 doi:10.1016/j.ijheatmasstransfer.2016.05.013.

904 [14] K. Yaji, T. Yamada, M. Yoshino, T. Matsumoto, K. Izui, S. Nishiwaki,
905 Topology optimization in thermal-fluid flow using the lattice Boltzmann

method, Journal of Computational Physics 307 (2016) 355–377 (feb 2016). doi:10.1016/j.jcp.2015.12.008.
URL http://dx.doi.org/10.1016/j.jcp.2015.12.008 http://linkinghub.elsevier.com/retrieve/pii/S0021999115008244

[15] F. Dugast, Y. Favennec, C. Josset, Y. Fan, L. Luo, Topology optimization of thermal fluid flows with an adjoint lattice boltzmann method, Journal of Computational Physics 365 (2018) 376 – 404 (2018). doi:https://doi.org/10.1016/j.jcp.2018.03.040.
URL http://www.sciencedirect.com/science/article/pii/S0021999118302067

[16] F. Okkels, H. Bruus, Scaling behavior of optimally structured catalytic microfluidic reactors, Physical Review E - Statistical, Nonlinear, and Soft Matter Physics 75 (1) (2007). arXiv:0608020, doi:10.1103/PhysRevE.75.016301.

[17] D. Schäpper, R. Lencastre Fernandes, A. E. Lantz, F. Okkels, H. Bruus, K. V. Gernaey, Topology optimized microbioreactors, Biotechnology and Bioengineering 108 (4) (2011) 786–796 (2011). doi:10.1002/bit.23001.

[18] K. Yaji, S. Yamasaki, S. Tsushima, T. Suzuki, K. Fujita, Topology optimization for the design of flow fields in a redox flow battery, Structural and Multidisciplinary Optimization 57 (2) (2018) 535–546 (2018). doi:10.1007/s00158-017-1763-8.

[19] C. Kim, H. Sun, Topology optimization of gas flow channel routes in an automotive fuel cell, International Journal of Automotive Technology 13 (5) (2012) 783–789 (aug 2012). doi:10.1007/s12239-012-0078-4.
URL http://link.springer.com/article/10.1007/s12239-012-0027-2 http://link.springer.com/10.1007/s12239-012-0078-4

[20] D. Makhija, G. Pingen, R. Yang, K. Maute, Topology optimization of multi-component flows using a multi-relaxation time lattice Boltzmann method, Computers and Fluids 67 (2012) 104–114 (2012). doi:10.1016/j.compfluid.2012.06.018.

[21] G. Allaire, F. Jouve, A.-M. Toader, A level-set method for shape optimization, Comptes Rendus Mathematique 334 (12) (2002) 1125–1130 (2002). arXiv:1010.1724, doi:10.1016/S1631-073X(02)02412-3.
URL http://linkinghub.elsevier.com/retrieve/pii/S1631073X02024123

[22] T. Yamada, K. Izui, S. Nishiwaki, A. Takezawa, A topology optimization method based on the level set method incorporating a fictitious interface energy, Computer Methods in Applied Mechanics and Engineering 199 (2010) 2876–2891 (2010). doi:10.1016/j.cma.2010.05.013.

[23] S. Succi, R. Benzi, F. Higuera, The lattice Boltzmann equation: A new tool for computational fluid-dynamics, Physica D: Nonlinear Phenomena 47 (1-2) (1991) 219–230 (jan 1991). doi:10.1016/0167-2789(91)90292-H.
URL http://www.sciencedirect.com/science/article/pii/016727899190292H

[24] Q. Zou, X. He, On pressure and velocity flow boundary conditions and bounceback for the lattice Boltzmann BGK model, Physics of Fluids 9 (6) (1996) 1591–1598 (nov 1996). arXiv:9611001, doi:10.1063/1.869307.
URL http://arxiv.org/abs/comp-gas/9611001\nhttp://scitation.aip.org/content/a
http://aip.scitation.org/doi/10.1063/1.869307
http://arxiv.org/abs/comp-gas/9611001
http://dx.doi.org/10.1063/1.869307

[25] G. Pingen, A. Evgrafov, K. Maute, Topology optimization of flow domains using the lattice Boltzmann method, Structural and Multidisciplinary Optimization 34 (2007) 507–524 (2007). doi:10.1007/s00158-007-0105-7.

[26] F. Klemens, B. Förster, M. Dorn, G. Thäter, M. J. Krause, Solving fluid flow domain identification problems with adjoint lattice boltzmann methods, Computers & Mathematics with Applications (2018).

[27] F. Klemens, S. Schuhmann, G. Guthausen, G. Thäter, M. J. Krause, Cfd-mri: A coupled measurement and simulation approach for accurate fluid flow characterisation and domain identification, Computers & Fluids 166 (2018) 218–224 (2018).

[28] K. Yaji, T. Yamada, M. Yoshino, T. Matsumoto, K. Izui, S. Nishiwaki, Topology optimization using the lattice Boltzmann method incorporating level set boundary expressions, Journal of Computational Physics 274 (2014) 158–181 (oct 2014). doi:10.1016/j.jcp.2014.06.004.
URL http://www.sciencedirect.com/science/article/pii/S0021999114004112

[29] G. Liu, M. Geier, Z. Liu, M. Krafczyk, T. Chen, Discrete adjoint sensitivity analysis for fluid flow topology optimization based on the generalized lattice Boltzmann method, Computers & Mathematics with Applications 68 (10) (2014) 1374–1392 (nov 2014). doi:10.1016/j.camwa.2014.09.002.
URL http://www.sciencedirect.com/science/article/pii/S0898122114004507

[30] C. Obrecht, F. Kuznik, B. Tourancheau, J. J. Roux, Multi-GPU implementation of the lattice Boltzmann method, Computers and Mathematics with Applications 65 (2) (2013) 252–261 (2013). doi:10.1016/j.camwa.2011.02.020.
URL http://dx.doi.org/10.1016/j.camwa.2011.02.020

[31] N. Delbosc, Real-Time Simulation of Indoor Air Flow Using the Lattice Boltzmann Method on Graphics Processing Unit (September) (2015).

[32] F. Dugast, Optimisation topologique en convection thermique avec la méthode Lattice Boltzmann, Ph.D. thesis, Université de Nantes (2018).

[33] H. Liu, Q. Kang, C. R. Leonardi, S. Schmieschek, A. Narváez, B. D. Jones, J. R. Williams, A. J. Valocchi, J. Harting, Multiphase lattice Boltzmann simulations for porous media applications, Computational Geosciences 20 (4) (2016) 777–805 (2016). arXiv:1404.7523, doi:10.1007/s10596-015-9542-3.
URL http://link.springer.com/10.1007/s10596-015-9542-3

[34] Y. Yan, Y. Zu, Numerical simulation of heat transfer and fluid flow past a rotating isothermal cylinder – A LBM approach, International Journal of Heat and Mass Transfer 51 (9-10) (2008) 2519–2536 (may 2008). doi:10.1016/j.ijheatmasstransfer.2007.07.053.
URL http://linkinghub.elsevier.com/retrieve/pii/S001793100700573X

[35] L. Li, R. Mei, J. F. Klausner, Lattice Boltzmann models for the convection-diffusion equation: D2Q5 vs D2Q9, International Journal of Heat and Mass Transfer 108 (2017) 41–62 (2017). doi:10.1016/j.ijheatmasstransfer.2016.11.092.
URL http://linkinghub.elsevier.com/retrieve/pii/S0017931016326047

[36] G. R. McNamara, A. L. Garcia, B. J. Alder, Stabilization of thermal lattice Boltzmann models, Journal of Statistical Physics 81 (1-2) (1995)

395–408 (oct 1995). doi:10.1007/BF02179986.
URL http://link.springer.com/10.1007/BF02179986

[37] S. Ponce Dawson, S. Chen, G. D. Doolen, Lattice boltzmann computations for reaction-diffusion equations, The Journal of Chemical Physics 98 (2) (1993) 1514–1523 (1993). arXiv:https://doi.org/10.1063/1.464316, doi:10.1063/1.464316.
URL https://doi.org/10.1063/1.464316

[38] J. R. Weimar, J. P. Boon, Nonlinear reactions advected by a flow, Physica A: Statistical Mechanics and its Applications 224 (1) (1996) 207 – 215, dynamics of Complex Systems (1996). doi:https://doi.org/10.1016/0378-4371(95)00355-X.
URL http://www.sciencedirect.com/science/article/pii/037843719500355X

[39] G. Allaire, O. Pantz, Structural optimization with FreeFem++, Structural and Multidisciplinary Optimization 32 (3) (2006) 173–181 (2006).

[40] S. Osher, J. A. Sethian, Front propagating with courvature-dependent speed: algorithms based on hamilton-Jacoby formulations, J. Computational physics 79 (1988) 12–49 (1988). doi:10.1016/0021-9991(88)90002-2.
URL E:\BIBLIO\Articles\Front-propagating-curvature-dependent-speed_Osher_1988

[41] S. Osher, N. Paragios, Geometric Level Set Methods in Imaging, Vision, and Graphics, Springer-Verlag New York, Inc., Secaucus, NJ, USA, 2003 (2003).

[42] J. A. Sethian, A. Wiegmann, Structural Boundary Design via Level Set and Immersed Interface Methods, Journal of Computational Physics 163 (2000) 489–528 (2000). doi:10.1006/jcph.2000.6581.
URL http://www.scopus.com/inward/record.url?eid=2-s2.0-0001176192&partnerID=4

[43] M. Y. Wang, X. Wang, D. Guo, A level set method for structural topology optimization, Computer Methods in Applied Mechanics and Engineering 192 (1-2) (2003) 227–246 (jan 2003). doi:10.1016/S0045-7825(02)00559-5.
URL http://www.sciencedirect.com/science/article/pii/S0045782502005595

[44] G. Allaire, F. D. Gournay, F. Jouve, A.-M. Toader, Structural optimization using topological and shape sensitivity via a level set method,

Control and cybernetics 34 (October 2004) (2005) 59 (2005).
URL http://oxygene.ibspan.waw.pl:3000/contents/export?filename=2005-1-allaire

[45] A. Aghasi, M. Kilmer, E. L. Miller, Parametric level set methods for inverse problems, SIAM Journal on Imaging Sciences 4 (2) (2011) 618–650 (2011).

[46] D. a. Wolf-Gladrow, Lattice-Gas Cellular Automata and Lattice Boltzmann Models - An Introduction, PoLAR (2000) 308 (2000).
URL http://books.google.com/books?hl=en&lr=&id=cHcpWgxAUu8C&oi=fnd&pg=PA15&dq

[47] S. Succi, The Lattice Boltzmann Equation for Fluid Dynamics and Beyond, Vol. 222, 2001 (2001). doi:10.1016/0370-1573(92)90090-M.
URL http://linkinghub.elsevier.com/retrieve/pii/037015739290090M

[48] Y. H. Qian, D. d'Humières, P. Lallemand, Lattice BGK Models for Navier-Stokes Equation, EPL (Europhysics Letters) 17 (1992) 479 (1992).
URL http://stacks.iop.org/0295-5075/17/i=6/a=001

[49] P. Bhatnagar, E. Gross, M. Krook, A Model for Collision Processes in Gases. I. Small Amplitude Processes in Charged and Neutral One-Component Systems, Physical Review 94 (3) (1954) 511–525 (may 1954). doi:10.1103/PhysRev.94.511.
URL http://link.aps.org/doi/10.1103/PhysRev.94.511

[50] S. Marié, Etude de la méthode Boltzmann sur Réseau pour les simulations en aéroacoustique, Thèse UPMC (2008) 170 (2008).

[51] D. d'Humières, Multiple-relaxation-time lattice Boltzmann models in three dimensions (2002) 437–451 (2002). doi:10.1098/rsta.2001.09.

[52] Z. Liu, A. Song, L. Xu, W. Feng, L. Zhou, A High Scalable Hybrid MPI / OpenMP Parallel Model of Multiple-relaxation-time Lattice Boltzmann Method Multiple-relaxation-time Lattice Boltzmann Method 20 (91330116) (2014) 10147–10157 (2014). doi:10.12733/jcis12520.

[53] M. Tekitek, M. Bouzidi, F. Dubois, P. Lallemand, Adjoint lattice Boltzmann equation for parameter identification, Computers & Fluids 35 (8-9) (2006) 805–813 (sep 2006). doi:10.1016/j.compfluid.2005.07.015.
URL http://linkinghub.elsevier.com/retrieve/pii/S0045793005001428

[54] H. Xu, O. Malaspinas, P. Sagaut, Sensitivity analysis and determination of free relaxation parameters for the weakly-compressible mrt-lbm schemes, Journal of Computational Physics 231 (21) (2012) 7335 – 7367 (2012). doi:https://doi.org/10.1016/j.jcp.2012.07.005.
URL http://www.sciencedirect.com/science/article/pii/S0021999112003646

[55] Q. Zou, S. Hou, S. Chen, G. D. Doolen, A improved incompressible lattice Boltzmann model for time-independent flows, Journal of Statistical Physics 81 (1-2) (1995) 35–48 (oct 1995). doi:10.1007/BF02179966.
URL http://link.springer.com/10.1007/BF02179966

[56] X. He, L.-S. Luo, Lattice Boltzmann Model for the Incompressible Navier-Stokes Equation, Journal of Statistical Physics 88 (1997) 927–944 (1997). doi:10.1023/B:JOSS.0000015179.12689.e4.
URL http://www.springerlink.com/openurl.asp?id=doi:10.1023/B:JOSS.0000015179.

[57] S. Chen, G. D. Doolen, Lattice Boltzmann method for fluid flows, Annual review of fluid mechanics 30 (1) (1998) 329–364 (jan 1998). doi:10.1098/rsta.2011.0109.
URL http://www.annualreviews.org/doi/abs/10.1146/annurev.fluid.30.1.329

[58] P. Lallemand, L.-S. Luo, Theory of the lattice Boltzmann method: Dispersion, dissipation, isotropy, Galilean invariance, and stability, Physical Review E 61 (6) (2000) 6546–6562 (jun 2000). doi:10.1103/PhysRevE.61.6546.
URL http://link.aps.org/doi/10.1103/PhysRevE.61.6546

[59] R. Mei, L. S. Luo, P. Lallemand, D. d'Humières, Consistent initial conditions for lattice Boltzmann simulations, Computers and Fluids 35 (8-9) (2006) 855–862 (2006). doi:10.1016/j.compfluid.2005.08.008.

[60] P. J. Dellar, Lattice Boltzmann algorithms without cubic defects in Galilean invariance on standard lattices, Journal of Computational Physics 259 (2014) 270–283 (2014). doi:10.1016/j.jcp.2013.11.021.
URL http://dx.doi.org/10.1016/j.jcp.2013.11.021

[61] Z. Chai, B. Shi, Z. Guo, A Multiple-Relaxation-Time Lattice Boltzmann Model for General Nonlinear Anisotropic Convection-Diffusion Equations, Journal of Scientific Computing 69 (1) (2016) 355–390 (2016). doi:10.1007/s10915-016-0198-5.

[62] I. Rasin, S. Succi, W. Miller, A multi-relaxation lattice kinetic method for passive scalar diffusion, Journal of Computational Physics 206 (2) (2005) 453–462 (2005). doi:10.1016/j.jcp.2004.12.010.

[63] G. Pingen, D. Meyer, Topology optimization for thermal transport, In: Proceedings of the ASME fluids engineering division summer conference 1 (PTS A-C) (2009) 2237–2243 (2009).
URL http://proceedings.asmedigitalcollection.asme.org/proceeding.aspx?article

[64] T. Inamuro, M. Yoshino, H. Inoue, R. Mizuno, F. Ogino, A Lattice Boltzmann Method for a Binary Miscible Fluid Mixture and Its Application to a Heat-Transfer Problem, Journal of Computational Physics 179 (2002) 201–215 (2002). doi:10.1006/jcph.2002.7051.
URL http://www.sciencedirect.com/science/article/pii/S0021999102970518

[65] M. Gunzburger, Adjoint equation-based methods for control problems in incompressible, viscous flows, Flow, Turbulence and Combustion 65 (3-4) (2000) 249–272 (2000). doi:10.1023/A:1011455900396.
URL http://link.springer.com/article/10.1023/A:1011455900396

[66] T. Bruns, Topology optimization of convection-dominated, steady-state heat transfer problems, International Journal of Heat and Mass Transfer 50 (15-16) (2007) 2859–2873 (jul 2007). doi:10.1016/j.ijheatmasstransfer.2007.01.039.
URL http://www.sciencedirect.com/science/article/pii/S0017931007001330

[67] J. Liu, A multiresolution method for distributed parameter estimation, SIAM Journal on Scientific Computing 14 (2) (1993) 389–405 (1993).

[68] F. Dubot, Y. Favennec, B. Rousseau, D. R. Rousse, A wavelet multi-scale method for the inverse problem of diffuse optical tomography, Journal of Computational and Applied Mathematics 289 (2015) 267–281 (2015).

[69] T. Liu, A wavelet multiscale method for the inverse problem of a non-linear convection–diffusion equation, Journal of Computational and Applied Mathematics 330 (2018) 165–176 (2018).

[70] G. Chavent, Nonlinear least squares for inverse problems: theoretical foundations and step-by-step guide for applications, Springer Science & Business Media, 2010 (2010).